A WIND AND RAIN BACKSCATTER MODEL DERIVED FROM AMSR AND SEAWINDS DATA

by

Seth N. Nielsen

A thesis submitted to the faculty of

Brigham Young University

in partial fulfillment of the requirements for the degree of

Master of Science

Department of Electrical and Computer Engineering

Brigham Young University

August 2007

BRIGHAM YOUNG UNIVERSITY

GRADUATE COMMITTEE APPROVAL

of a thesis submitted by

Seth N. Nielsen

This thesis has been read by each member of the following graduate committee and by majority vote has been found to be satisfactory.

Date	David G. Long, Chair
Date	Karl F. Warnick
Date	Travis E. Oliphant

BRIGHAM YOUNG UNIVERSITY

As chair of the candidate's graduate committee, I have read the thesis of Seth N. Nielsen in its final form and have found that (1) its format, citations, and bibliographical style are consistent and acceptable and fulfill university and department style requirements; (2) its illustrative materials including figures, tables, and charts are in place; and (3) the final manuscript is satisfactory to the graduate committee and is ready for submission to the university library.

Date

David G. Long
Chair, Graduate Committee

Accepted for the Department

Michael J. Wirthlin
Graduate Coordinator

Accepted for the College

Alan R. Parkinson
Dean, Ira A. Fulton
College of Engineering and Technology

ABSTRACT

A WIND AND RAIN BACKSCATTER MODEL DERIVED FROM AMSR AND SEAWINDS DATA

Seth N. Nielsen

Department of Electrical and Computer Engineering

Master of Science

The SeaWinds scatterometers aboard the QuikSCAT and ADEOS II satellites were originally designed to measure wind vectors over the ocean by exploiting the relationship between wind-induced surface roughening and the normalized radar backscatter cross-section. Recently, an algorithm for simultaneously retrieving wind and rain (SWR) from scatterometer measurements was developed that enables SeaWinds to correct rain-corrupted wind measurements and retrieve rain rate data. This algorithm is based on co-locating Tropical Rainfall Measuring Mission Precipitation Radar (TRMM PR) and SeaWinds on QuikSCAT data. In this thesis, a new wind and rain radar backscatter model is developed for the SWR algorithm using a global co-located data set with rain data from the Advanced Microwave Scanning Radiometer (AMSR) and backscatter data from the SeaWinds scatterometer aboard the Advanced Earth Observing Satellite 2 (ADEOS II). The model includes the effects of phenomena such as backscatter due to wind stress, atmospheric rain attenuation, and effective rain backscatter. Rain effect parameters of the model vary with integrated rain rate,

which is defined as the product of rain height and rain rate. This study accounts for rain height in the model in order to calculate surface rain rate from the integrated rain rate. A simple model for the mean rain height versus latitude and longitude is proposed based on AMSR data and methods of incorporating this model into the SWR retrieval process are developed. The performance of the new SWR algorithm is measured by comparison of wind vectors and rain rates to the previous SWR algorithm, AMSR rain rates, and NCEP numerical weather prediction winds. The new SWR algorithm produces accurate rain estimates and detects rain with a low false alarm rate. The wind correction capabilities of the SWR algorithm are effective at correcting rain-induced inaccuracies. A qualitative comparison of the wind and rain retrieval for Hurricane Isabel demonstrates these capabilities.

ACKNOWLEDGMENTS

I would like to thank Dr. David Long for his guidance throughout this study. I appreciate now that he did not simply give me all the answers, but allowed me to discover them for myself. I want to thank my children, Hannah and Joshua, for making me smile. I express my love for my wife, Rebecca, and am grateful for her encouragement, her love, and for her reminding me what my life's most important work is.

Contents

List of Tables

List of Figures

Chapter 1

Introduction

The oceans distribute the energy of the sun globally to make the Earth inhabitable. In order to understand and effectively predict climate world wide, scientists study the Earth's oceans to observe the interaction between these massive bodies of water and the atmosphere. Wind and rain are two phenomena that arise from this interaction and the accurate measurement of both has long been a pursuit of the scientific community. One of the most effective means of measuring wind and rain frequently and on a global scale is satellite-based remote sensing and more specifically, microwave wind scatterometry and radiometry [1].

A scatterometer is an active remote sensing device or radar that measures the radar backscatter cross-section, σ^o, of the ocean's surface. Ocean wind speed and direction can be retrieved by relating these σ^o measurements to the surface roughness of the ocean caused by wind stress. A radiometer is a passive remote sensor that measures the electromagnetic energy, also called brightness temperature, radiated by warm objects. Radiometers have many applications in remote sensing and the measurement of rain is one for which they are particularly effective. Rain is retrieved from radiometer brightness temperature measurements at various frequencies and polarizations. Water vapor, cloud water, and rain water are estimated by means of the physical relationship between them and the various brightness temperature measurements [2].

Rain has been a source of error in scatterometer-based wind retrieval because of the way it interferes with the radar beam. Rain-contaminated scatterometer measurements have generally been flagged and discarded in the past. However, given a

suitable backscatter model of the wind and rain, rain rate information can be retrieved while simultaneously improving the wind estimates of scatterometer wind retrieval [3]. This procedure is known as the simultaneous wind and rain retrieval and it has important implications for the utility of scatterometers.

The Advanced Earth Observing Satellite II (ADEOS II), launched in late 2002, carried both a SeaWinds scatterometer and a rain-measuring Advanced Microwave Scanning Radiometer (AMSR). The ADEOS II, shown in Figure 1.1, covered the entire globe and took co-located scatterometer and radiometer measurements for a little over six months before the satellite critically failed in October of 2003. This large set of co-located measurements provides an ideal means of studying the effect rain has on scatterometer measurements on a global scale.

Figure 1.1: The ADEOS II satellite.

1.1 Previous Work

The SeaWinds scatterometers on both ADEOS II and QuikSCAT have been shown to retrieve highly accurate wind vectors for most conditions over the Earth's oceans [4, 5]; however, the performance of the wind retrieval is severely degraded when rain is present [6, 7]. Many studies have been conducted on the effects of rain on radar backscatter especially as it applies to scatterometer-based wind retrieval, e.g. [7, 8, 9, 10]. The effect rain has on the observed backscatter is complicated and depends on the rain rate and wind speed among other factors, but in general, rain tends to increase the backscatter causing the retrieved wind speed to appear greater than the true wind speed [11]. Rain-corrupted wind tends to point orthogonal to the satellite track or cross swath regardless of the true wind direction [12]. Rain-contaminated scatterometer measurements are generally discarded when determining the accuracy of SeaWinds' retrieved wind vectors. Algorithms have been developed to flag scatterometer data for rain by thresholding a modified objective function of the σ^o observations [13, 14] or by using a multidimensional histogram involving several rain-sensitive parameters [12]. Some studies have developed wind and rain backscatter models in order to improve wind retrieval by separating the rain-induced backscatter from wind-induced backscatter. Stiles and Yueh developed a backscatter model by determining an affine relationship between the measured σ^o and the wind-only σ^o. The slope and intercept of the relationship were related to Special Sensor Microwave/Imager (SSM/I) integrated rain rates via linear regression [15]. Hilburn et al derived a wind and rain backscatter model using co-located data from AMSR and SeaWinds data on ADEOS II. Their synergistic model combines active and passive remote sensor data to correct scatterometer wind estimates in the presence of rain [16].

Draper and Long also incorporated such a model [7] into a simultaneous wind and rain retrieval (SWR) algorithm [3], which is capable of extracting wind and rain data from scatterometer measurements alone; however, the algorithm does not perform as well in latitudes outside the tropical region (between 35°N and 35°S latitude). The original model which Draper and Long developed for the SWR algorithm used

co-located data from the SeaWinds scatterometer on QuikSCAT and the Precipitation Radar on the Tropical Rainfall Measuring Mission (TRMM PR), which only covered the tropical region [7]. Thus, since rain parameters vary with latitude, the accuracy of the model decreases outside of this region.

1.2 Proposed Work

The purpose of this thesis is to develop a wind and rain backscatter model derived from the data of SeaWinds and AMSR on ADEOS II, incorporate this model into the SWR algorithm, and validate the model and algorithm. This new model is based on the same phenomenological backscatter model used by Draper and Long to represent the effects of rain on SeaWinds backscatter with two major differences: the rain data for this study is provided by AMSR, a radiometer, as opposed to the TRMM PR and the rain height is considered. By using data from SeaWinds and AMSR on the same platform, a larger co-located data set and and a broader range of latitudes are included in the derivation of the model parameters. The model's rain parameters are a function of integrated rain rate; however, rain storm height is estimated as well in order to provide the surface rain rate. The backscatter model is a closed form function of wind-only backscatter, rain rate, and rain height. The wind-only backscatter is derived from interpolating and projecting winds from the National Center for Environmental Prediction (NCEP) through the geophysical model function (GMF). The rain rate and the rain-induced parameters are derived from the co-located measurements of SeaWinds and AMSR aboard ADEOS II. The purpose of developing a new wind/rain backscatter model based on AMSR-derived rain data is to calibrate the SWR algorithm to retrieve rain rates comparable to those of AMSR. This will allow SeaWinds on QuikSCAT to measure rain rates on a global scale, thus extending the usefulness of the QuikSCAT mission which has no rain-measuring device.

1.3 Thesis Outline

This thesis is organized into six chapters. Chapter 2 gives a brief background on wind scatterometry and simultaneous wind/rain scatterometry. A more detailed

description of the remote sensing instruments and their corresponding data sets is also included.

Chapter 3 describes the method of deriving the new wind and rain backscatter model. Some of the limitations of the model and the data sets used are discussed and some techniques to mitigate these limitations are presented as well.

Chapter 4 is a discussion of rain storm height and its relevance to the SWR algorithm. The statistics of rain height are presented along with various methods of incorporating this data into the SWR algorithm.

Chapter 5 shows how well the updated SWR algorithm performs compared to other data sets. Its rain retrieval capabilities are compared to AMSR and its wind retrieval capabilities are compared to NCEP winds and the non-SWR SeaWinds retrieved winds. The performance of the new SWR algorithm is compared to the previous SWR algorithm in nearly all cases. A qualitative example of Hurricane Isabel is presented and examined.

Chapter 6 summarizes the key results of this study, discusses contributions, and potential research topics for future studies.

Chapter 2

Background, Instruments, and Data

This chapter provides background on scatterometry as it applies to wind and simultaneous wind/rain retrieval. The SeaWinds and AMSR instruments are described in terms of their basic operation aboard the ADEOS II. The data sets generated by SeaWinds, AMSR, and NCEP are also presented.

2.1 Wind Scatterometry

A scatterometer is a radar that sends pulses of electromagnetic energy at its target and then measures the return power in order infer some quality of the target. The amount of received power, P_r, is governed by the radar equation [17]

$$P_r = \frac{P_t G^2 \lambda^2 A_{eff}}{(4\pi)^3 R^4} \sigma^o \tag{2.1}$$

where P_t is the transmitted power, G is the antenna gain, λ is the operating wavelength, A_{eff} is the effective area of the target (essentially the area of the SeaWinds footprint), and R is the slant range from the radar to the target. Note that Equation 2.1 is idealized in that it assumes 100% radiation efficiency and the atmosphere does not attenuate the pulse. The only unknown in this equation is σ^o which is what a scatterometer measures very precisely when all the other quantities are known and the assumptions just mentioned are valid. σ^o depends on many factors such as the incidence angle of the beam, the orientation and roughness of the target with respect to the wavelength, as well as its dielectric properties.

Bragg resonance explains much of the interaction between the ocean surface and the scatterometer beam [17]. When wind blows over the surface of the ocean,

its momentum is transferred to the water, creating centimeter-scaled capillary waves. The spacing of these capillary waves is roughly the same as the Bragg wavelength causing the signal scattered off neighboring crests to add in phase, thus enhancing the return power and backscatter. As the surface becomes rougher, the backscatter increases. The roughness of the ocean's surface is directly proportional to the wind speed, thus σ^o increases with wind speed. The wind direction relative to the azimuth or look angle of the radar also modulates the values of σ^o and this dependence is symmetric about 180° relative azimuth angle. Figure 2.1 demonstrates the backscatter's dependence on wind speed and direction for the SeaWinds scatterometer.

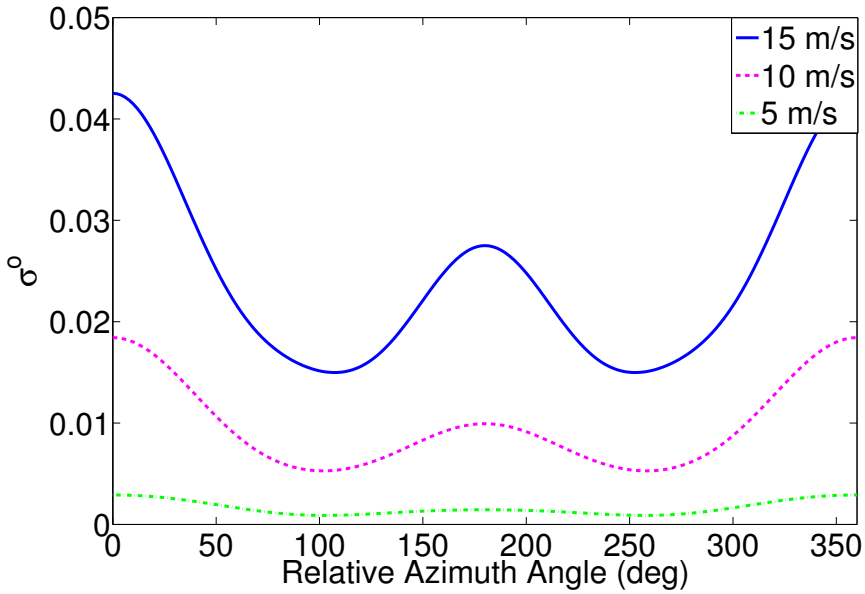

Figure 2.1: SeaWinds σ^o as a function of relative azimuth angle for wind speeds of 5, 10, and 15 m/s. The incidence angle in all cases is 46°.

Scatterometer-based wind retrieval over the ocean is made possible by the relationship between σ^o and the surface roughening caused by wind stress; this relationship is known as the geophysical model function (GMF) [17, 18]. The GMF, $\mathcal{M}$, is an empirical function that relates σ^o to the wind speed, s, relative azimuth angle,

χ, incidence angle, θ, and the frequency, f, and polarization of the SeaWinds beam, pol, [18]

$$\begin{aligned}\sigma^o &= \mathcal{M}(s, \chi, \theta, f, \text{pol}) \\ &= \mathcal{M}(\mathbf{u}, \theta).\end{aligned} \tag{2.2}$$

The shorter notation of (2.2) is used throughout the thesis for brevity. $\mathbf{u} = (s, \chi)$ is a common notation for the wind vector and for SeaWinds, there is only one operating frequency and the incidence angle implies the polarization of the σ^o measurement. The wind is retrieved by inverting the GMF through the use of maximum likelihood estimation (MLE).

Several σ^o measurements are made in a given scatterometer resolution element known as a wind vector cell (WVC). If the measurements are assumed to be independent and Gaussian-distributed, then the joint conditional probability function (pdf) of the σ^o measurements is

$$p(\mathbf{z}|\mathbf{u}) = \prod_k \frac{1}{\sqrt{2\pi\varsigma_k^2(\mathbf{u})}} \exp\left\{-\frac{1}{2}\frac{(z_k - \mathcal{M}_k(\mathbf{u}))^2}{\varsigma_k^2(\mathbf{u})}\right\} \tag{2.3}$$

where $\mathbf{z}$ is a vector of the σ^o observations, k is an index over all the observations in the WVC, $\mathcal{M}_k(\mathbf{u}) = \mathcal{M}(\mathbf{u}, \theta_k)$ is the model backscatter corresponding to the specific geometry of the kth observation, and ς_k^2 is the variance of the kth measurement. The SeaWinds likelihood function is derived by negating the log of (2.3) and ignoring additive and multiplicative constants,

$$l(\mathbf{z}|\mathbf{u}) = \sum_k \frac{(z_k - \mathcal{M}_k(\mathbf{u}))^2}{\varsigma_k^2(\mathbf{u})}. \tag{2.4}$$

For standard SeaWinds processing, the log of the variance term is ignored [19]. The MLE of the wind vector is obtained by finding $\mathbf{u}$ that minimizes (2.4) (equivalent to maximizing (2.3)),

$$\hat{\mathbf{u}}_{MLE} = \arg\min_{\mathbf{u}} \{l(\mathbf{z}|\mathbf{u})\}. \tag{2.5}$$

Due to the symmetry of the GMF and measurement noise, the likelihood function is non-linear and has multiple local minima or wind vector ambiguities that represent

possible wind vector solutions. Ambiguity selection is a process by which the ambiguities in neighboring WVCs are chosen to give an overall wind vector field closest to the true wind field. The first step in ambiguity selection uses an external reference wind field to pick the wind vector ambiguities closest to the reference field; this step is known as nudging [20]. Once the wind field has been nudged, a median filter is applied to the selected wind field in order to make its flow more consistent with itself [21].

2.2 Simultaneous Wind/Rain Scatterometry

Simultaneous wind and rain retrieval is a relatively recent development in the field of scatterometry [3]. It extends the wind-only GMF to include backscatter and attenuation effects of rain. The wind/rain GMF is

$$\begin{aligned} z_k &= \mathcal{M}_k(\mathbf{u})\alpha_r(R_{ir}) + \sigma_e(R_{ir}) \\ &= \mathcal{M}_{rk}(\mathbf{u}, R_{ir}) \end{aligned} \tag{2.6}$$

where z_k is the kth σ^o measurement and $\mathcal{M}_{rk}$ is the model backscatter corresponding to the viewing geometry of the kth measurement. The model parameters α_r and σ_e represent the rain attenuation and effective rain backscatter respectively and are functions of the integrated rain rate, R_{ir}. When there is no rain present in the WVC, then $\alpha_r = 1$ and $\sigma_e = 0$. The significance of these parameters is explained in more detail in Chapter 3.

Simultaneous wind and rain retrieval is performed in a similar manner to wind-only retrieval except a third parameter, the integrated rain rate (R_{ir}), is estimated. The conditional pdf of the observations is

$$p_r(\mathbf{z}|\mathbf{u}, R_{ir}) = \prod_k \frac{1}{\sqrt{2\pi\varsigma_{rk}^2(\mathbf{u}, R_{ir})}} \exp\left\{-\frac{1}{2}\frac{(z_k - \mathcal{M}_{rk}(\mathbf{u}, R_{ir}))^2}{\varsigma_{rk}^2(\mathbf{u}, R_{ir})}\right\} \tag{2.7}$$

and the likelihood function is

$$l_r(\mathbf{z}|\mathbf{u}, R_{ir}) = \sum_k \frac{(z_k - \mathcal{M}_{rk}(\mathbf{u}, R_{ir}))^2}{\varsigma_{rk}^2(\mathbf{u}, R_{ir})}. \tag{2.8}$$

The estimation procedure for $\mathbf{u}$ and R_{ir} is the same as in (2.5). However, estimating a third parameter increases the complexity of searching for local minima as well as computation time. Estimating a third parameter also increases the noisiness of the estimates, especially when it is not raining; however, simultaneous wind and rain retrieval has been shown to be sufficiently accurate in many wind and rain rate regimes [3, 22].

2.3 Instruments and Data Sets

The ADEOS II satellite, which carried SeaWinds and AMSR, had a sun-synchronous, near-polar orbit with an equatorial local crossing time of 10:30 AM. The satellite completed one revolution (rev) in 101 minutes with a repeat period of 4 days. The measurements of the two sensors are co-located in space except for the outermost portion of AMSR's swath and there is no more than 2.5 minutes between co-located measurements [16].

2.3.1 SeaWinds Scatterometer

The SeaWinds scatterometer is the most recent space-borne scatterometer designed by the National Aeronautics and Space Administration (NASA) and represents a significant departure from its predecessors, the SEASAT Active Scatterometer System of 1978 and the NASA scatterometer of 1996-1997. SeaWinds features circularly scanning pencil beams at fixed incidence angles; whereas, the previous scatterometers employed fixed fan beams. SeaWinds is a K_u-band scatterometer operating at a frequency of 13.4 GHz and employs two beams of different polarizations. The outer beam is vertically polarized (v-pol) with an incidence angle of 54° and the inner beam is horizontally polarized (h-pol) with an incidence angle of 46°. With a swath width of 1800 km, SeaWinds was able to cover about 90% of the Earth's surface daily aboard ADEOS II. The design of SeaWinds affords it unique benefits and challenges [23], especially in terms of its sensitivity to rain. A SeaWinds scatterometer was first launched on the QuikSCAT satellite in June 1999 and a second SeaWinds was

launched on ADEOS II in December 2002. The ADEOS II experienced an operation anomaly that subsequently caused the critical failure of the satellite in October 2003.

The resolution element of the standard SeaWinds processing is a 25 km $\times$ 25 km WVC. The σ^o measurements are stored in the level 2A data structure (L2A files). The L2A measurements are processed to produce the wind vectors which are stored in the level 2B data structure (L2B files). The L2B processed wind vector data for one rev is laid out in a grid of 76 $\times$ 1624 WVCs.

2.3.2 AMSR

The AMSR, designed by the Japan Aerospace Exploration Agency (JAXA), measures brightness temperatures at eight distinct frequencies in order to measure precipitation, sea surface temperature (SST), and water vapor among other geophysical parameters. The AMSR was another remote sensing instrument on board the ADEOS II during its brief period of operation. AMSR takes both v-pol and h-pol measurements for all frequencies except two. The antenna scans a semicircular pattern in front of the spacecraft at a fixed incidence angle of 55° giving AMSR a slightly wider swath (1900 km) than SeaWinds. Figure 2.2 illustrates the viewing geometries of SeaWinds and AMSR aboard ADEOS II.

The AMSR level 2A overlay (L2Ao files) report parameters such as rain rate and SST on a grid designed to overlay the SeaWinds L2B product. Due to its higher frequencies, AMSR products have a higher resolution than the SeaWinds L2B products. The AMSR overlay data is divided into 12.5 km $\times$ 12.5 km squares or wind vector cell quadrants (WVCQ), with four quadrants inside each L2B WVC. AMSR data is also used to empirically calculate the rain attenuation at SeaWinds' operating frequency. This rain attenuation measurement is contained in the SeaWinds L2A data structure for each σ^o measurement.

2.3.3 NCEP Numerical Weather Prediction Winds

This study also makes use of the NCEP model winds which are numerically predicted winds that are calculated every six hours with a very course resolution

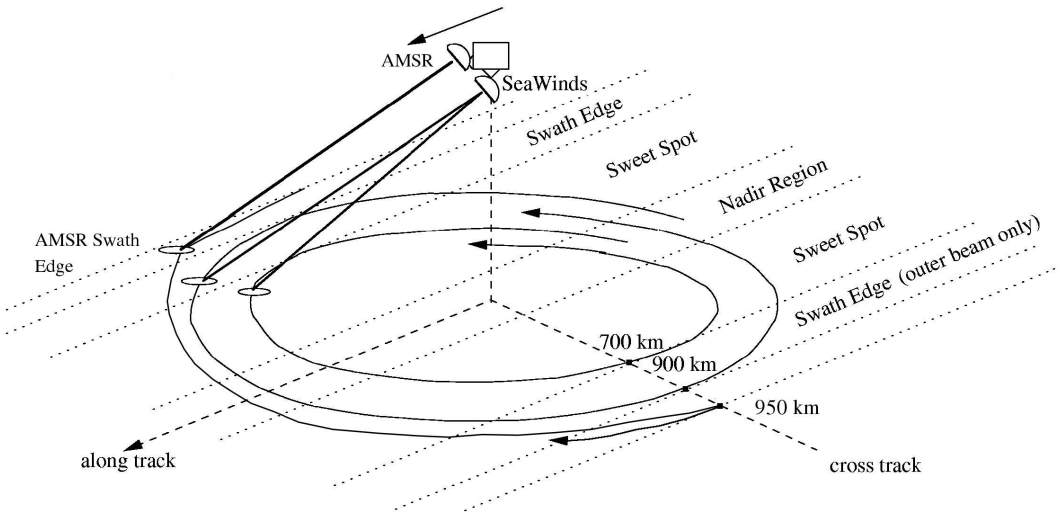

Figure 2.2: SeaWinds and AMSR measurement geometry aboard ADEOS II.

($2.5° \times 2.5°$). Because of this coarse resolution, small scale wind features and rain effects are not included in the prediction process, allowing us to obtain a rough estimate of the rain-free wind. These predicted winds are interpolated in space and time to each SeaWinds WVC; however, the NCEP winds are biased high when compared to the winds retrieved by SeaWinds [24]. The method for correcting this bias is presented in section 3.3.

Chapter 3

Wind and Rain Backscatter Model

Rain has three major effects on radar backscatter: raindrops roughen the ocean's surface, which tends to augment the surface backscatter, the raindrops falling in the atmosphere attenuate the radar signal as it travels to and from the ocean's surface, and atmospheric rain also scatters the signal. We model these rain-induced effects with a simple phenomenological model [3],

$$\sigma_m = (\sigma_w + \sigma_{sr})\alpha_r + \sigma_r \tag{3.1}$$

where σ_m is the backscatter measured by SeaWinds, σ_w is the surface backscatter from wind-induced capillary waves, σ_{sr} is the surface backscatter due to raindrop splash products, α_r is the two-way atmospheric rain attenuation, and σ_r is the volume scattering due to atmospheric rain.

The three rain-effect parameters, σ_{sr}, α_r, and σ_r are functions of the rain rate and rain height. The σ_{sr} term is a simplified model for the average rain-induced surface perturbation effect which ignores the interaction between wind and rain. Since we are only interested in the bulk effect of surface perturbation due to rain, an additive parameter is sufficient. The atmospheric rain parameters (α_r and σ_r) ignore certain sources of variability such as drop size distribution and vertical profile. These effects are small, and so they are not explicitly included in the model for the sake of simplicity. To further simplify the backscatter model of (3.1), we combine the rain effects into a more compact model,

$$\sigma_m = \sigma_w \alpha_r + \sigma_e \tag{3.2}$$

where $\sigma_e = \sigma_{sr}\alpha_r + \sigma_r$ is the effective rain backscatter. This model is useful for studying the bulk effect of rain on backscatter, because it combines three sources of uncertainty into two.

3.1 Rain Model Parameter Extraction

We use data in the AMSR L2Ao files and the SeaWinds L2A files to compute rain model parameters. As indicated before, AMSR rain rate data in the L2Ao files is reported on a grid; and therefore, must be interpolated to the center latitude and longitude of each SeaWinds σ^o observation in order to observe the effect rain has on backscatter. The rain rate for a given σ^o measurement is set to the value of the nearest neighboring AMSR WVCQ. Nearest-neighbor interpolation is done for simplicity, while a more rigorous method could use a weighted average of nearby cells based on the gain pattern of the antenna.

The viewing geometries of SeaWinds and AMSR are different in several ways and these differences affect the perceived rain attenuation of each instrument. The v-pol measurement of SeaWinds has an incidence angle of 54° which is similar to AMSR's 55° incidence angle; however, SeaWinds' h-pol measurement has an incidence angle of 46°. The AMSR signal is subject to more attenuation compared to the h-pol measurement because AMSR detects a given point on the ground from farther away than the SeaWinds h-pol beam. SeaWinds' observations can be fore or aft with respect to the orientation of the spacecraft; whereas, AMSR only looks forward. Due to these discrepancies in viewing geometry, AMSR and SeaWinds observe somewhat different scenes when rain is present. The AMSR rain attenuation is computed empirically for each σ^o observation and so the difference in incidence angles is implicitly taken into account [25]. The difference in azimuth observation angle relative to the spacecraft is not addressed in computing the rain attenuation.

Partial beam-filling is not explicitly accounted for in estimating the model parameters. Partial beam-filling occurs when the horizontal extent of a rain storm is smaller than the width of the radar beam passing through it. It is intuitive that the rain attenuation of the beam is greater if the beam is completely filled by a rain storm

as opposed to being only partially filled by a smaller storm where both storms have the same rain rate. Correcting for partial beam-filling from SeaWinds data alone is difficult. Hilburn et al. account for partial beam-filling in their ocean wind correction algorithm by means of an effective temperature depression, which is calculated from AMSR brightness temperatures [16]. Draper and Long discuss the problem of partial beam-filling in [7]; however, it is not explicitly included in their approach. They instead demonstrate that the worst case difference in σ_e due to partial beam-filling is 4 dB. Such a case is extremely rare and the difference is generally much smaller. This suggests that good results can be obtained without explicitly correcting for partial beam-filling.

3.2 Relating Rain Parameters to Integrated Rain Rate

Using AMSR-derived measurements of the surface rain rate and rain attenuation for each σ^o observation, a relationship between the two can be established. Figure 3.1 shows a plot of atmospheric rain attenuation versus rain rate. While a relationship between rain rate and attenuation is apparent some other factor is modulating this dependence, which explains the multiple linear populations and spreading. The total atmospheric attenuation (i.e. from all sources), τ, of the scatterometer signal can be expressed as

$$\tau = 2 \int_0^{r_o} (\kappa_g + \kappa_{ec} + \kappa_{er}) dr, \tag{3.3}$$

where the factor of 2 indicates a two-way attenuation, r_o is the distance from the observation point to the scatterometer and κ_g, κ_{ec}, and κ_{er} are the extinction coefficients of atmospheric gases, clouds, and rain respectively expressed in dB/m [17]. During a rain event, we assume that κ_{er} is much larger than the other terms in (3.3) so that τ is roughly equal to α_r in dB. For simplicity, we assume that κ_{er} is uniform from the surface up to the rain height, h_r, since we are interested only in the net rain effects. Based on these assumptions,

$$\tau \approx \int_0^{h_r} \kappa_{er} dr = h_r \kappa_{er} \tag{3.4}$$

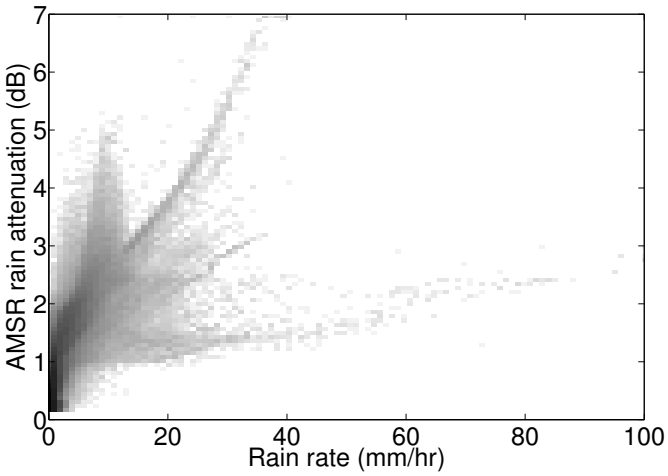

Figure 3.1: Atmospheric rain attenuation (dB) versus rain rate (mm/hr) for the h-pol beam.

where the factor of 2 in Equation(3.3) is absorbed in κ_{er}. This approximation of the atmospheric attenuation is related to rain rate by

$$\kappa_{er} = \kappa_1 R_r^b \tag{3.5}$$

where R_r is the rain rate and κ_1 and b are wavelength-dependent constants [17]. For K_u band, $b \approx 1$, yielding a simple approximation for τ in terms of the rain rate,

$$\tau \approx \kappa_1 h_r R_r, \tag{3.6}$$

i.e. the rain attenuation is proportional to the product of rain rate and rain height. Equation (3.6) is modified for an off-nadir-looking radar by multiplying by the secant of the incidence angle.

The product of rain rate and rain height is related to the integrated rain rate under a simple assumption. Integrated rain rate, measured in units of km mm/hr, is defined as

$$R_{ir} = \int_0^{h_r} R_r(z) dz \tag{3.7}$$

where R_r is the rain rate as a function of distance. For the remainder of the paper, the rain rate is assumed to be constant throughout the height of the storm for all

σ^o measurements in the same WVC, so that the integrated rain rate is the simple product of rain rate and rain height,

$$R_{ir} \approx \int_0^{h_r} R_r dz = h_r R_r. \tag{3.8}$$

By substituting (3.8) into (3.6), the atmospheric attenuation is

$$\tau \approx \kappa_1 R_{ir}, \tag{3.9}$$

indicating that attenuation is a function of integrated rain rate.

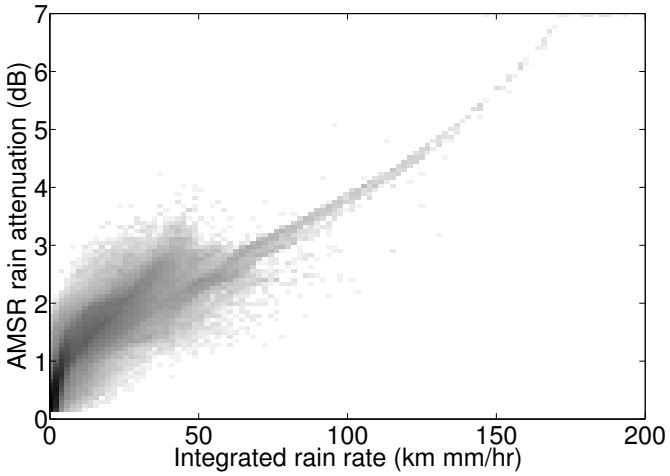

Figure 3.2: Scatter density plot of atmospheric rain attenuation (dB) versus integrated rain rate (km mm/hr) for the h-pol beam.

In order to compute the integrated rain rate, we must have estimates of the rain height for each σ^o observation. Using a technique similar to that of [2], data from the AMSR L2Ao files is used to estimate the rain height [26]. We determine rain height for each σ^o observation by assigning it the rain height of the nearest WVCQ. We multiply the AMSR-derived rain rate and rain height to obtain the integrated rain rate and plot the rain attenuation versus integrated rain rate, shown in Figure 3.2. Although there is much variability in the attenuation at lower rain rates, there is

significantly less spreading of the data in this plot. The correlation coefficient of the data in Figure 3.1 is 0.71 while the correlation coefficient of the data in Figure 3.2 is 0.83. The AMSR rain attenuation was estimated based on columnar liquid, water vapor, and sea surface temperature and not directly from rain rate, which explains the spread in the data at low rain rates. The correlation between integrated rain rate and rain attenuation is much clearer at high rain rates, so we conclude that rain rate and rain height are the most significant sources of variability in the rain attenuation.

3.3 Estimation of Wind-only Backscatter and Bias Correction

The wind-only backscatter term, σ_w, of Equation (3.2) represents the backscatter due to wind if no rain were present. In order to derive the model parameters, σ_w is estimated from the NCEP model winds contained in the SeaWinds L2B product. The NCEP winds are interpolated to the center latitude and longitude of each SeaWinds σ^o measurement by performing a cubic spline interpolation of the orthogonal wind vector components separately. The interpolated vector components are recombined to obtain the speed and direction of the wind vectors, which are then projected through the GMF in order to estimate the wind-only backscatter at each σ^o egg location,

$$\sigma_{w(NCEP)} = \mathcal{M}(s_{(NCEP)}, \chi_{(NCEP)}, \theta, \text{pol}), \tag{3.10}$$

where $\mathcal{M}$ represents the GMF, $s_{(NCEP)}$ is the interpolated NCEP wind speed, $\chi_{(NCEP)}$ is the relative azimuth angle of the interpolated NCEP wind vector, θ is the incidence angle, and pol is the beam polarization.

$\sigma_{w(NCEP)}$ is a biased estimate of the actual σ_w because the NCEP winds themselves are biased relative to SeaWinds winds as mentioned previously. Due to the low resolution of NCEP winds, we assume the bias is spatially correlated. We estimate the bias, ϵ, for each σ^o observation as a weighted average of the difference between σ_m and σ_w for all rain-free observations in the same look direction, either fore or aft. We define rain-free observations as those whose rain rate is less than 0.01 mm/hr because 0.01 mm/hr is the lowest rain rate reported in the AMSR data. The bias error of the

jth observation is

$$\epsilon^j = \frac{\sum_i W^{ij} \left(\sigma^i_{m(SW)} - \sigma^i_{w(NCEP)} \right)}{\sum_i W^{ij}} \tag{3.11}$$

where the index i sums over all rain-free observations of the same look direction as the jth observation and $\sigma^i_{m(SW)}$ is the backscatter measured by SeaWinds. W^{ij} is the Epanechnikov weighting function for the ith and jth observations, which is calculated by,

$$W^{ij} = \begin{cases} 1 - \left(\frac{d(i,j)}{r} \right)^2, & d(i,j) \leq r \\ 0, & \text{otherwise} \end{cases} \tag{3.12}$$

where r is a radius in km around the jth observation and $d(i,j)$ is the distance between the ith and jth observations in km. Nominally, r is 20 km unless there are less than two observations within 20 km, in which case, the radius is dilated by adding 10 km at a time until at least two observations are found within the radius. σ_w can now be written as the sum of the backscatter predicted from the NCEP winds and the bias error,

$$\sigma_w = \sigma_{w(NCEP)} + \epsilon. \tag{3.13}$$

The mean bias is -0.0021 with a standard deviation of 0.0052 which is consistent with the observation that NCEP winds are biased slightly high compared to SeaWinds winds. These values are comparable to a mean of -0.0025 and standard deviation of 0.0064 observed in [7] for QuikSCAT data.

3.4 Relating Rain Model Parameters to Integrated Rain Rate

Estimates of the effective rain backscatter can be computed using the estimates of wind-only backscatter and rain attenuation by rearranging the terms in Equation (3.2),

$$\sigma_e = \sigma_m - (\sigma_{w(NCEP)} + \epsilon)\alpha_{r(AMSR)}. \tag{3.14}$$

The rain model parameters of Equation (3.2) are calculated and related to integrated rain rate for each σ^o measurement. We model atmospheric rain attenuation and

effective rain backscatter as quadratic polynomials of integrated rain rate:

$$10\log_{10}(-(\alpha_{r(AMSR)})_{dB}) \approx f_a(R_{ir}) = \sum_{n=0}^{2} c_a(n) R_{ir}^n, \tag{3.15}$$

$$(\sigma_e)_{dB} \approx f_e(R_{ir}) = \sum_{n=0}^{2} c_e(n) R_{ir}^n, \tag{3.16}$$

where R_{ir} is the integrated rain rate in dB. α_r is converted to dB twice in (3.15) in order to facilitate fitting the data with a quadratic polynomial, similar to [7].

The training data set used to calculate the model parameters include data from the L2A, L2Ao, and L2B files and is composed of one rev selected randomly from each day of the ADEOS II mission. In order to avoid sea-ice contamination near the poles, only data found in regions between 60° S and 60° N latitude are included. R_{ir} is calculated from the AMSR L2Ao files, the $\alpha_{r(AMSR)}$ term is taken from the SeaWinds L2A file (note that it is calculated based on AMSR data even though it is found in the SeaWinds data set [25]), and the $\sigma_{w(NCEP)}$ and ϵ terms are derived from the NCEP winds found in the SeaWinds L2B files. Roughly 5 million co-located data points are used to calculate the h-pol parameter coefficients and 3 million are used to calculate the v-pol coefficients. We solve for the quadratic polynomial coefficients c_a and c_r by casting Equations (3.15) and (3.16) into matrix form and using a least-squares pseudo-inverse. These coefficients are recorded in Table 3.1 for both h-pol and v-pol observations. These attenuation and effective rain backscatter models are valid for integrated rain rates between 0.01 km mm/hr and 100 km mm/hr. The full wind and rain backscatter model is

$$\begin{aligned}\sigma_m(s,d,R_{ir}) &= \sigma_w(s,d)\alpha_r(R_{ir}) + \sigma_e(R_{ir}) \\ &= \sigma_w(s,d)10^{-10^{f_a(R_{ir})/10}/10} + 10^{f_e(R_{ir})/10},\end{aligned} \tag{3.17}$$

where s and d are the wind speed and direction.

Figures 3.3 and 3.4 show plots comparing the rain model parameters to those of Draper and Long [7]. For the remainder of the paper we refer to the model in [7] as the DL SWR model and our model is referred to as the AMSR SWR model. The range of values are comparable for both parameters and both polarizations; however,

Table 3.1: Coefficients of the quadratic fits to the parameters α_r and σ_e in Equations (3.15) and (3.16) respectively.

	$c_a(0)$	$c_a(1)$	$c_a(2)$
h-pol	-9.2879	1.0379	-0.0151
v-pol	-9.0998	1.1747	-0.022
	$c_e(0)$	$c_e(1)$	$c_e(2)$
h-pol	-28.69	1.0817	-0.0197
v-pol	-27.3168	0.7168	-0.0106

the behavior of the two models is slightly different. For the scales shown in the plot of Figure 3.3, the DL SWR attenuation model appears nearly linear; whereas, the AMSR SWR attenuation model appears somewhat parabolic. The attenuation values for the AMSR SWR model are lower than those of the DL SWR model for the lowest and the highest integrated rain rates. The fact that the attenuation values of the AMSR SWR model appear to level off at higher rain rates is probably due to the effect of partial beam-filling for the empirically calculated attenuation values. Higher rain rates tend to represent convective storm systems [25, 27] whose physical scale is between 5 and 10 km [28]; therefore, they only partially fill the SeaWinds' footprint, which is 24 km $\times$ 31 km for the smaller inner beam [29]. This suggests that on average the partial beam-filling effect is accounted for by the empirical calculation of the attenuation. A similar trend is also seen in the σ_e models where the effective rain backscatter tends to level off at higher rain rates for the AMSR SWR model suggesting that the partial beam-filling effect is accounted for in σ_e. For increasing integrated rain rates, σ_e is larger for the h-pol beam than it is for the v-pol beam, which has been noted in previous investigations [15, 7].

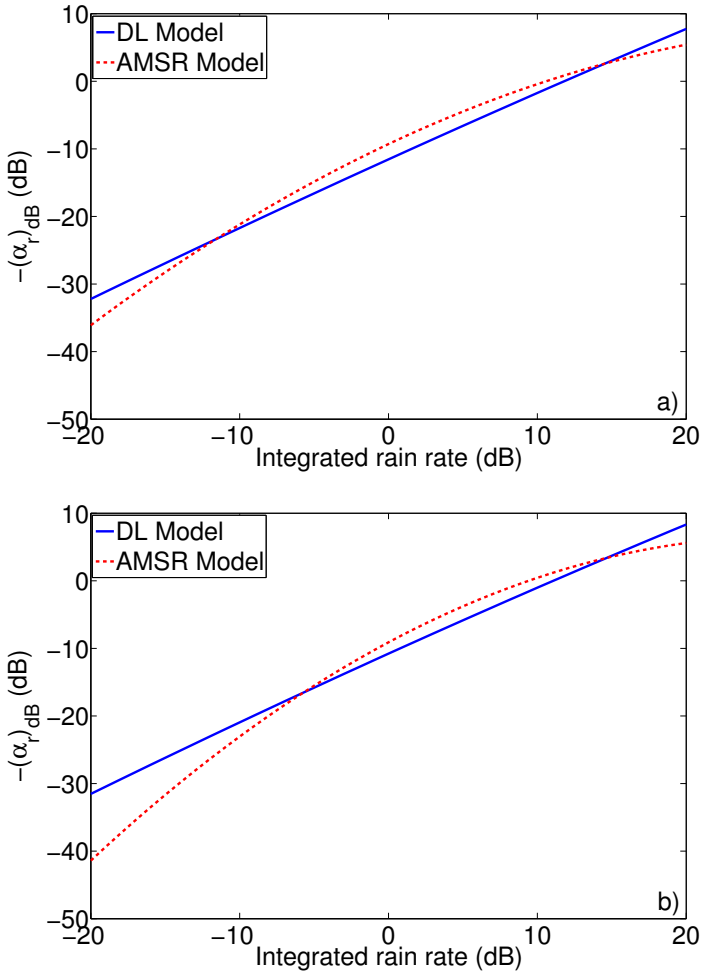

Figure 3.3: Model atmospheric rain attenuation versus integrated rain rate for the a) h-pol and b) v-pol beams.

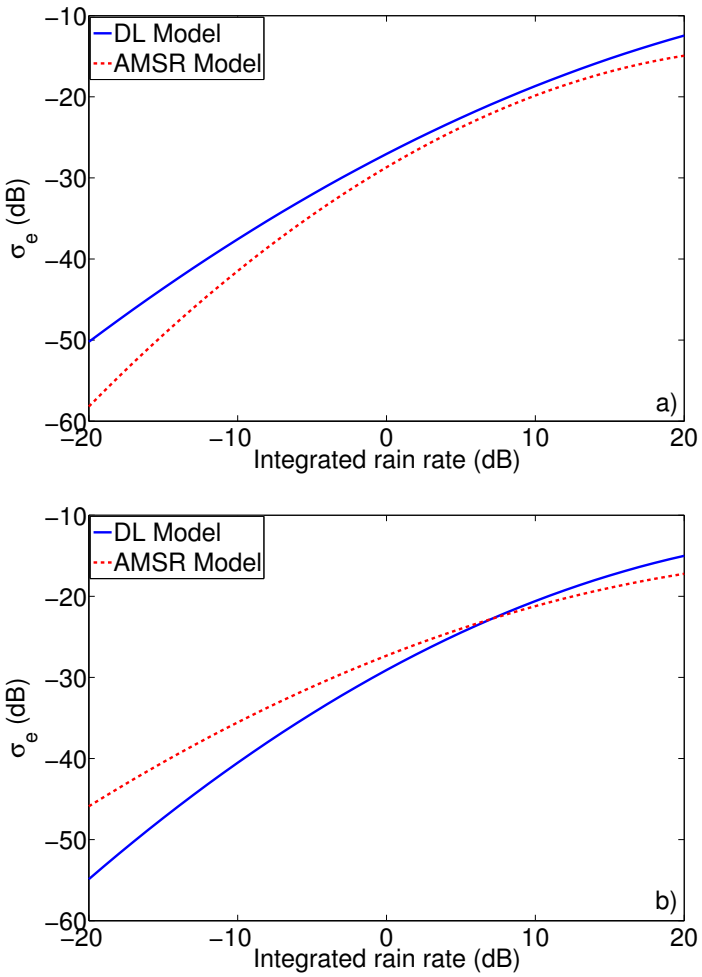

Figure 3.4: Model effective rain backscatter versus integrated rain rate for the a) h-pol and b) v-pol beams.

Chapter 4

Rain Height

The SWR algorithm estimates an irregularly weighted spatial average *integrated* rain rate for each WVC [3]. AMSR estimates rain rate, so in order to compare the two methods of rain retrieval, an estimate of the rain height is necessary to convert integrated rain rate to surface rain rate. SeaWinds was designed to measure the normalized radar backscatter cross-section, so it has no range resolution and therefore cannot measure rain height from the time of flight of the first radar return. Since the rain height cannot be directly estimated by SeaWinds, it must be provided by a climatological model. The following sections examine the statistics of the rain height and the different methods of incorporating rain height into the SWR algorithm.

4.1 Rain Height Statistics

Studies have shown that rain height is a function of latitude, longitude, and season [30, 31] and the AMSR-derived rain heights demonstrate these dependences. Figure 4.1a shows a plot of rain height versus latitude. The bands that occur at discrete rain heights are due to the quantization of the AMSR data used to calculate the rain heights. This figure demonstrates a strong connection between rain height and latitude; however, there is a great deal of spread in the rain heights for a given latitude bin. The non-parametric fit to the data represents the mean rain height of each latitude bin. The mean rain height is small in the higher latitudes and reaches a peak near the equator. This trend can be modeled using a polynomial in latitude. Figure 4.1b shows that the variance of the rain height also depends on latitude. It

is worth noting that the variance of the rain height increases with distance from the equator, a phenomenon that has been observed in previous studies [30, 31].

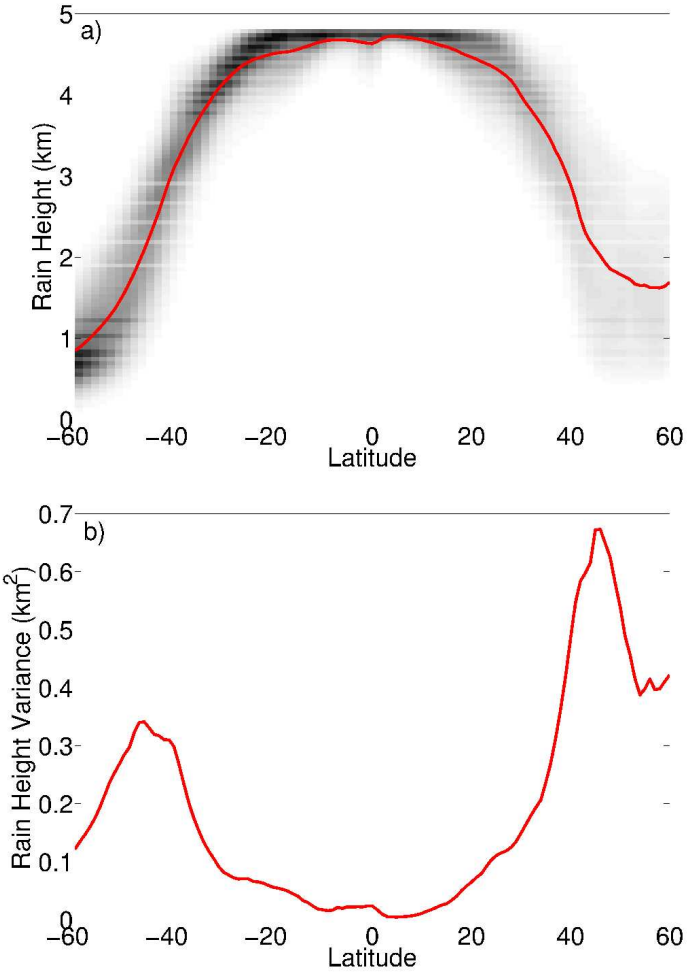

Figure 4.1: a) Rain height versus latitude and a non-parametric approximation of the mean rain height. b) Rain height variance versus latitude. Rain heights are derived from AMSR SST data. Bin centers are spaced 0.5° apart.

Rain height also varies with time and longitude. Figure 4.2 demonstrates the time dependence of rain height by showing mean rain height with respect to latitude for two days representing two different seasons. The two plots show that the mean rain height shifts in latitude over time with an especially large shift in the northern

latitudes. Figure 4.3 is a map of average global rain heights for the entire ADEOS II mission, which demonstrates how the rain height varies with longitude.

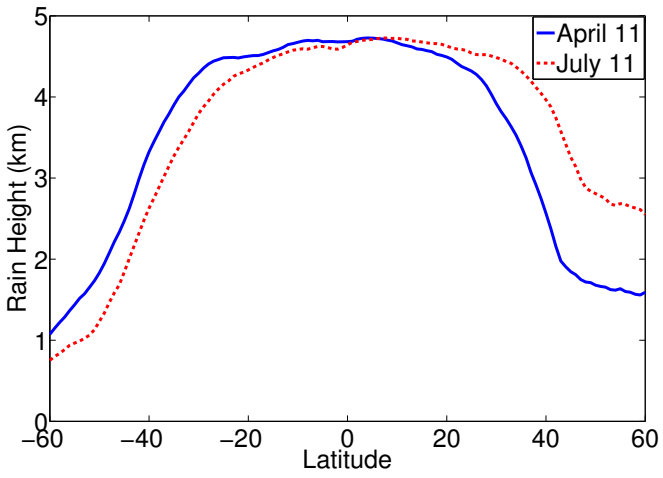

Figure 4.2: Non-parametric approximation of rain height versus latitude for different seasons.

Mean rain height tables based on different combinations of latitude, longitude, and Julian day are created and compared based on how much they account for the variance of the rain height. Let σ_h^2 be the variance of the rain height for the entire ADEOS II mission and let σ_i^2 be the variance of the height difference, which is the rain height minus the rain height estimated from the ith table. The fraction of the variance that the ith table accounts for is simply $1 - \sigma_i^2/\sigma_h^2$. A summary of these statistics for the different tables is presented in Table 4.1. Latitude is the largest factor for determining rain height, accounting for nearly 90% of the variance in the rain height by itself. The most complete model includes all three index parameters and accounts for 97% of the variance. The combination of latitude and longitude marginally outperforms the combination of latitude and day, both accounting for roughly 92% of the variance.

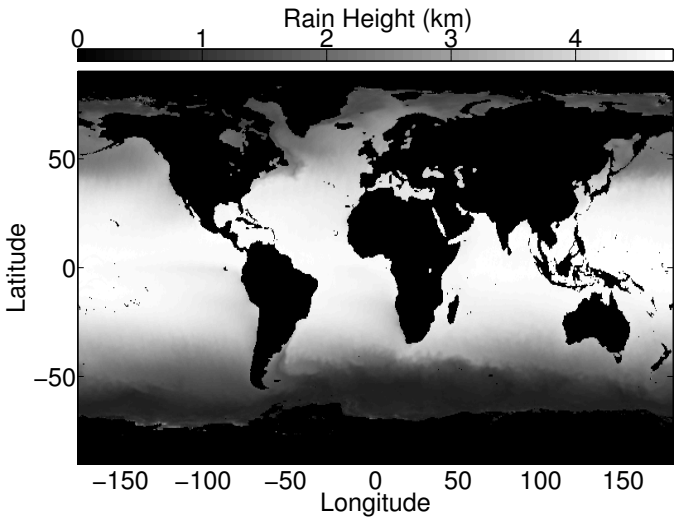

Figure 4.3: Global average rain heights for the ADEOS II mission.

Since the ADEOS II failed before a full year's worth of data could be acquired, the rain height statistics are limited to the months between April and October. Because of this temporal gap in the rain height data, we cannot form a rain height table that is indexed by day for use outside of these months. Thus, we ignore seasonal dependence for the remainder of the study and use the table based only on latitude and longitude. We note that the gap in temporal rain height data limits the accuracy of the latitude and longitude rain height maps because the mean rain height is biased towards the values of the summer months. Future work to improve the rain height table should use a larger data set of rain heights to generate the climatological rain height maps.

4.2 Incorporating Rain Height into the SWR Algorithm

The SWR algorithm uses maximum likelihood estimation (MLE) to retrieve wind vector and integrated rain rate ambiguities from the σ^o observations [3]. In order to retrieve the surface rain rate, rain height must be incorporated into the estimation process. Three similar simultaneous wind/rain estimation techniques to do this are presented in the sections that follow. All three techniques are based on maximum a

Table 4.1: Variance of the rain height differences for the various mean rain height tables.

Table No.	Index Parameters	Variance	% of variance accounted for
h	-	2.08	0%
1	Lat.	0.23	88.9%
2	Lat. Day	0.17	91.8%
3	Lat. Lon.	0.16	92.1%
4	Lat. Lon. Day	0.06	97.3%

posteriori (MAP) estimation and differ only in the assumptions made about the prior distributions. The first method is the most general and the second and third methods are simplifications of the first method based on certain assumptions. The advantages and disadvantages of these methods are discussed and the third method is selected for use in the AMSR SWR algorithm.

4.2.1 Method 1: Rain Rate and Rain Height MAP Estimation

One method of retrieving rain rate is to use MLE to simultaneously estimate rain rate and rain height instead of the integrated rain rate, thus making the objective function a function of wind speed and direction ($\mathbf{u}$), rain rate (R_r), and rain height (h_r):

$$l_r(\mathbf{z}|\mathbf{u}, R_r, h_r) = \sum_k \frac{(z_k - \mathcal{M}_{rk}(\mathbf{u}, R_r, h_r))^2}{\varsigma^2_{rk}(\mathbf{u}, R_r, h_r)}, \tag{4.1}$$

Table 4.2: Correlation coefficients of various combinations of the estimation parameters of Equation (4.3). s and d are the wind speed and direction respectively.

	$(R_r)_{dB}$	h_r	s	d
$(R_r)_{dB}$	-	-0.39	0.28	-0.13
h_r	-0.39	-	-0.49	0.35
s	0.28	-0.49	-	-0.15
d	-0.13	0.35	-0.15	-

where $\mathbf{z}$ is a vector of the σ^o measurements. The disadvantage of using an MLE in this case is that there are nearly infinite combinations of rain rate and rain height that yield the same integrated rain rate. Without some method of selecting the appropriate rain height, there would be countless solutions that minimize the MLE objective function; MAP estimation provides a solution to this problem. Based on the discussion of Section 4.1, prior distributions of the rain height for a given latitude, longitude, and day can be calculated. These prior distributions of the rain height can be used in a MAP estimator of $\mathbf{u}$, R_r, and h_r. The posterior distribution of $\mathbf{u}$, R_r, and h_r given $\mathbf{z}$ is

$$p(\mathbf{u}, R_r, h_r|\mathbf{z}) = \frac{p(\mathbf{z}|\mathbf{u}, R_r, h_r)p(\mathbf{u}, R_r, h_r)}{p(\mathbf{z})} \tag{4.2}$$

and the MAP estimator of the parameters $\mathbf{u}$, R_r, and h_r is

$$\begin{aligned}(\hat{\mathbf{u}}, \hat{R_r}, \hat{h_r})_{MAP} &= \underset{(\mathbf{u},R_r,h_r)}{\arg\max}\{p(\mathbf{u}, R_r, h_r|\mathbf{z})\} \\ &= \underset{(\mathbf{u},R_r,h_r)}{\arg\max}\{p(\mathbf{z}|\mathbf{u}, R_r, h_r)p(\mathbf{u}, R_r, h_r)\}\end{aligned} \tag{4.3}$$

where the term $p(\mathbf{z})$ is discarded since it is constant with respect to the arguments $\mathbf{u}$, R_r, and h_r.

The joint distribution $p(\mathbf{u}, R_r, h_r)$ in Equation (4.3) can be computed empirically; however, in order to take advantage of the prior distribution of the rain height without unnecessarily constraining the wind vector or rain rate, two assumptions are made. First, $\mathbf{u}$, R_r, and h_r are assumed to be mutually independent, so that the joint distribution of these parameters is a product of the individual distributions,

$p(\mathbf{u}, R_r, h_r) = p(\mathbf{u})p(R_r)p(h_r)$. The assumption of independence cannot be proved without knowing the true probability densities, but we can compute the correlation coefficients of the different combinations of $\mathbf{u}$, R_r, and h_r, as shown in Table 4.2. The largest correlation coefficient (in magnitude) is only 0.49, so there does not appear to be any appreciable correlation between any of the estimation parameters. We note that one study found a positive correlation between rain rate and rain height in TRMM PR data [32]; however, this does not appear to be the case for AMSR data. Although such low correlation does not prove statistical independence, it suggests that the assumption is reasonable. The second assumption is that the prior distributions of $\mathbf{u}$ and R_r are uniform over their range of possible values. This assumption is made in order to simplify the estimation procedure because we do not need to provide prior distributions for $\mathbf{u}$ or R_r.

These assumptions are applied to equation (4.3):

$$\begin{aligned}(\hat{\mathbf{u}}, \hat{R_r}, \hat{h_r})_{MAP} &= \underset{(\mathbf{u},R_r,h_r)}{\arg\max}\{p(\mathbf{z}|\mathbf{u}, R_r, h_r)p(\mathbf{u})p(R_r)p(h_r)\} \\ &= \underset{(\mathbf{u},R_r,h_r)}{\arg\max}\{p(\mathbf{z}|\mathbf{u}, R_r, h_r)p(h_r)\}. \end{aligned} \tag{4.4}$$

Maximizing the log of (4.4) is equivalent to minimizing its negative,

$$(\hat{\mathbf{u}}, \hat{R_r}, \hat{h_r})_{MAP} = \underset{(\mathbf{u},R_r,h_r)}{\arg\min}\{-\log(p(\mathbf{z}|\mathbf{u}, R_r, h_r)) - \log(p(h_r))\}. \tag{4.5}$$

For the sake of simplicity, if h_r is assumed to be Gaussian-distributed with known mean and variance, its log-distribution can be written as

$$\log(p(h_r)) = -\frac{1}{2}\log(2\pi\sigma_h^2) - \frac{1}{2}\frac{(h_r - \mu_h)^2}{\sigma_h^2}. \tag{4.6}$$

Substituting (4.6) and (4.1) into (4.5) and discarding the additive constants and common multiplicative constant terms, we obtain the final form of the MAP estimator,

$$(\hat{\mathbf{u}}, \hat{R_r}, \hat{h_r})_{MAP} = \underset{(\mathbf{u},R_r,h_r)}{\arg\min}\left\{ l_r(\mathbf{z}|\mathbf{u}, R_r, h_r) + \frac{(h_r - \mu_h)^2}{\sigma_h^2} \right\}, \tag{4.7}$$

where l_r is the MLE objective function of Equation (4.1).

The assumption that h_r is Gaussian-distributed leads to an elegant solution; nevertheless, it is not completely accurate. Figure 4.4 shows three AMSR rain height

histograms at different latitudes (0°, 30° N, and 50° N), each accompanied by a Gaussian pdf fit. The histograms at 30° N and 50° N have roughly a Gaussian shape; however, the histogram at 0° latitude has a large concentration of rain heights near 4.8 km, which is the maximum rain height. In this case the Gaussian approximation is not as reasonable. If more accuracy is required for the distribution of h_r, then empirical pdfs can be used instead of applying the Gaussian assumption.

4.2.2 Method 2: Mean Height as a Fixed MLE Parameter

In order to simplify the estimator of Equation (4.7), we assume h_r is a degenerate random variable with a delta function distribution centered at the mean rain height, μ_h, such that $p(h_r) = \delta(h_r - \mu_h)$. Under this assumption,

$$\begin{aligned}(\hat{\mathbf{u}}, \hat{R_r}, \hat{h_r}) &= \arg\max_{(\mathbf{u},R_r,h_r)}\{p(\mathbf{z}|\mathbf{u}, R_r, h_r)p(h_r)\} \\ &= \arg\max_{(\mathbf{u},R_r,h_r)}\{p(\mathbf{z}|\mathbf{u}, R_r, h_r)\delta(h_r - \mu_h)\} \end{aligned} \tag{4.8}$$

and

$$(\hat{\mathbf{u}}, \hat{R_r}, \hat{h_r} = \mu_h) = \arg\max_{(\mathbf{u},R_r)}\{p(\mathbf{z}|\mathbf{u}, R_r, \mu_h)\}, \tag{4.9}$$

which after some manipulation becomes

$$(\hat{\mathbf{u}}, \hat{R_r})_{MLE} = \arg\min_{(\mathbf{u},R_r)}\{l_r(\mathbf{z}|\mathbf{u}, R_r, h_r = \mu_h)\}. \tag{4.10}$$

This is essentially a MLE of $\mathbf{u}$ and R_r using the mean rain height as a fixed parameter. In this case, the rain height is a constant used to compute the integrated rain rate that is an input to the combined wind and rain GMF, $\mathcal{M}_{rk}(\mathbf{u}, R_{ir} = \mu_h R_r)$. This simplification of the estimation problem does not require much modification of the SWR algorithm; instead of searching for integrated rain rate, we search for rain rate.

4.2.3 Method 3: Mean Height as a Scale Factor

The second method can be simplified further by using the SWR algorithm to estimate R_{ir} using Equation (2.8) as the objective function. Based on (3.8), the rain rate is the integrated rain rate divided by the mean rain height, or $R_r = R_{ir}/\mu_h$.

4.2.4 Comparison of Methods

The MAP estimator presented as method 1 represents the full wind vector, rain rate, and rain height estimator; however, it has some drawbacks that limit its utility. This estimator requires searching for the local minima of a function of four variables which adds complexity to the original SWR algorithm and greatly increases the computation time required to search for the local minima. For these reasons, simulation of this method in order to compare its performance against the other two methods was impractical. Such a comparison is reserved for future investigation (see Section 6.1).

Simulations were performed on SeaWinds data using methods 2 and 3. These simulations revealed that the second and third method yield the same wind speed and direction ambiguities. The rain rate ambiguities of the two methods are not significantly different with the largest observed difference being about 0.0075 mm/hr. Essentially, methods 2 and 3 yield the same results; however, method 3 requires less modification of the SWR algorithm and is slightly faster to compute than method 2. These advantages make method 3 the preferred method of the two for incorporating rain height into the SWR algorithm. The algorithm is slightly modified to use the AMSR SWR wind/rain model and the latitude- and longitude-based table of mean rain heights discussed in Section 4.1. The validation of the AMSR SWR algorithm is presented in Chapter 5.

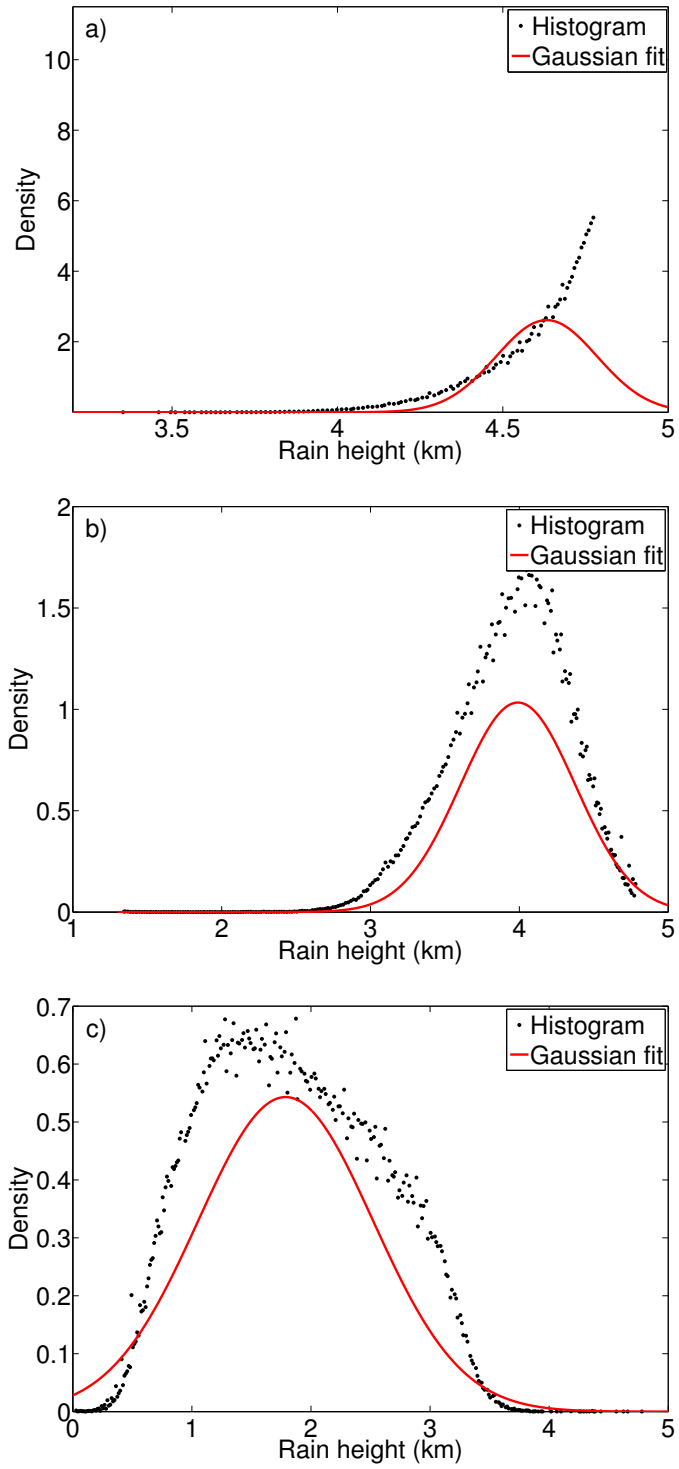

Figure 4.4: AMSR rain height histograms and Gaussian pdf fit for a) 0°, b) 30° N, and c) 50° N latitude. Latitude bins are 1° wide.

Chapter 5

Validation Results

To validate the performance of the AMSR SWR algorithm, data from the entire SeaWinds on ADEOS II mission are processed using the AMSR SWR algorithm. Results and statistics presented in this section are for the entire mission unless otherwise stated. The rain rates of the AMSR SWR algorithm are compared to AMSR rain rates and the wind vectors are compared to NCEP winds only in locations where AMSR, DL SWR, or AMSR SWR detects rain. In order to convert the DL SWR's integrated rain rates to surface rain rates, they are divided by the rain heights provided by the same rain height table used by AMSR SWR.

5.1 Rain Rate Comparison

This section compares AMSR SWR and DL SWR rain retrieval to that of AMSR rain estimates. Figure 5.1 shows a scatter density plot of AMSR rain rates versus AMSR SWR rain rates for May 2003. The rain rate thresholds discussed in [22] are used to discard rain rates that are deemed spurious. The data points of this scatter plot are concentrated above the equality line, indicating that the AMSR SWR rain rates are biased high compared to AMSR. The bias can be corrected by adjusting the rain model parameter coefficients of Table 3.1 according to the technique presented in [33]. The bias-corrected model coefficients are used for the rest of the thesis.

The ADEOS II mission is reprocessed using the bias-corrected rain model and the scatter density plots of DL SWR and AMSR SWR rain rates versus AMSR rain rates for May 2003 are presented in Figure 5.2. By comparing Figures 5.1 and 5.2b, the bias in the AMSR SWR rain rates is noticeably improved. For the data presented

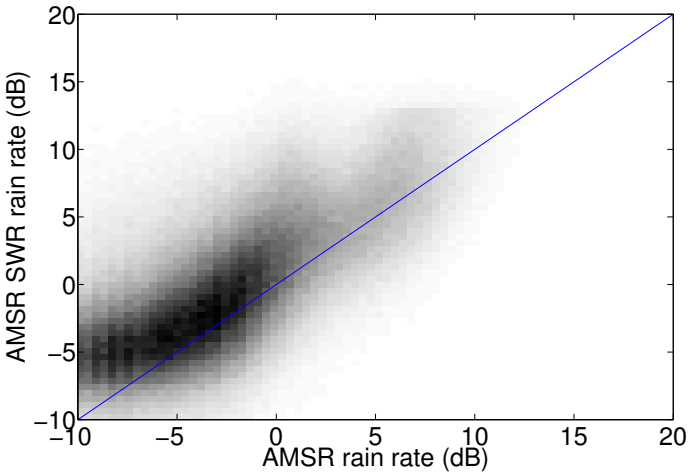

Figure 5.1: Scatter density plots of AMSR rain rates versus AMSR SWR rain rates for the month of May 2003. Rain rates are expressed in dB. The equality line is shown for comparison.

in Figure 5.2, the correlation coefficient of DL SWR with AMSR rain rates is 0.64 and the correlation coefficient of AMSR SWR with AMSR rain rates is 0.61. For the entire mission, the mean bias of DL SWR relative to AMSR rain rates is -0.86 mm/hr and the mean bias of AMSR SWR relative to AMSR rain rates is -0.55 mm/hr. Overall, the DL SWR rain rates have a higher correlation with AMSR's, but the AMSR SWR rain rates are less biased.

To demonstrate the SWR algorithm's ability to separate wind and rain effects on backscatter, each WVC is classified by backscatter regime, which is determined by the rain fraction defined as the ratio of effective rain backscatter to the total measured backscatter, $F = \sigma_e/\sigma_m$. Table 5.1 contains a summary of these backscatter regimes. The rain rate data sets are binned by backscatter regime and the correlation coefficient and the mean and RMS difference (in linear scale, not dB scale) are calculated for all regimes. These statistics are summarized in Table 5.2. The data in regime 2 have the highest correlation coefficients because rain dominates the backscatter and the rain estimates have a higher quality than the other regimes. The data in regime 0 has the lowest correlation coefficients because wind dominates the backscatter and

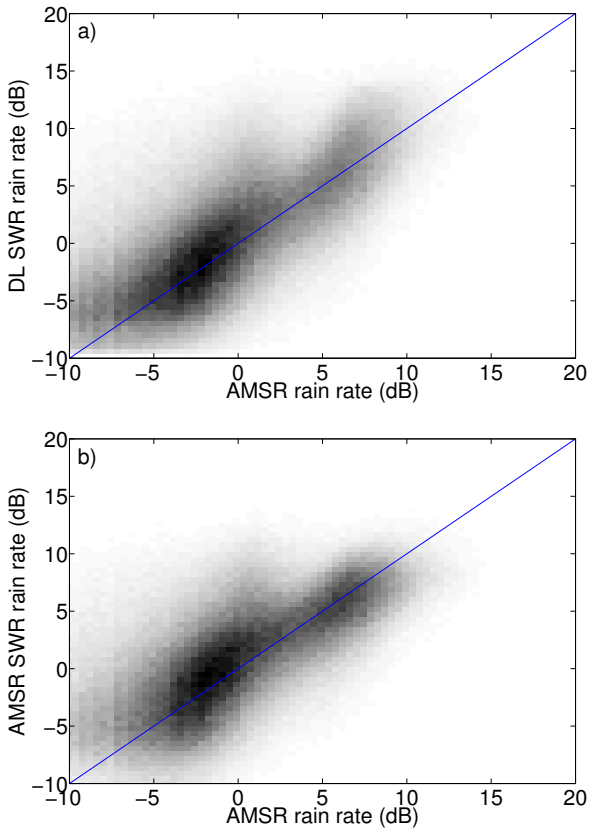

Figure 5.2: Scatter density plots from May 2003 of: a) AMSR rain rates versus DL SWR rain rates and b) AMSR rain rates versus AMSR SWR rain rates. Rain rates are expressed in dB. The equality line is shown for comparison.

degrades the quality of rain estimation. Essentially, rain estimation in this regime is unreliable. Overall, the AMSR SWR has lower mean and RMS differences relative to AMSR rain rates than the DL SWR. When the data is binned by regime, the DL SWR has the smallest mean and RMS differences in regime 0 and the differences increases with increasing regime. This trend goes against the intuition that suggests the precision and accuracy should be highest for regime 2 where rain dominates. The AMSR SWR follows this intuition more closely although regime 1 is somewhat more accurate than regime 2.

Figure 5.3 shows the average rain rate versus latitude for the month of June 2003. The AMSR SWR average rain rates resemble the AMSR rain rates more than

Table 5.1: Summary of backscatter regimes.

Regime No.	Rain Fraction $F = \sigma_e/\sigma_m$	Description
0	$F < 0.25$	Wind dominates backscatter
1	$0.25 \leq F \leq 0.75$	Wind and rain backscatter are comparable
2	$0.75 < F$	Rain dominates backscatter

the DL SWR rain rates except in the southernmost latitudes (between 40° and 60° S latitude) where the AMSR SWR rain rates become larger than AMSR's. The DL SWR average rain rates are larger than AMSR's and they become increasingly larger at 20° S latitude and below. This suggests that AMSR SWR has improved rain retrieval performance over a broader range of latitudes, even though it needs further improvement in latitudes south of 40° S.

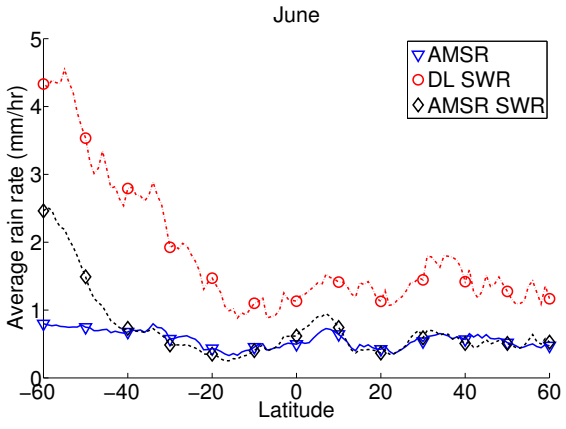

Figure 5.3: Average rain rates binned by latitude for AMSR, DL SWR, and AMSR SWR for June 2003.

Table 5.2: Correlation coefficients and mean and RMS differences for DL SWR and the AMSR SWR rain rates compared to AMSR rain rates. Correlation coefficients are computed for the dB rain rates while the mean and RMS differences are computed for linear scale rain rates. A negative difference indicates the SWR rain rates are larger than the AMSR rain rates on average.

Regime	Correlation coefficient		Mean difference (mm/hr)		RMS difference (mm/hr)	
	DL SWR	AMSR SWR	DL SWR	AMSR SWR	DL SWR	AMSR SWR
all	0.64	0.61	-0.86	-0.55	3.89	2.96
0	0.27	0.20	-0.1127	-1.08	1.953	3.613
1	0.57	0.54	-0.6098	-0.4465	3.564	3.165
2	0.81	0.74	-1.694	-0.6443	4.979	2.573

Overall, the AMSR SWR has improved rain retrieval capabilities compared to the DL SWR. Despite DL SWR's higher correlation with AMSR rain rates, AMSR SWR's rain rates are generally more accurate and precise. The accuracy of AMSR SWR rain estimates improves as the rain contributes significantly to the backscatter (regimes 1 and 2). The monthly average rain rates of AMSR SWR and AMSR are comparable for a broad range of latitudes; whereas, DL SWR's average rain rates are larger than AMSR's across all latitudes. The comparisons made in this section were primarily in areas where AMSR and AMSR SWR or AMSR and DL SWR both detected non-zero rain. The next section compares the ability of the DL and AMSR SWR algorithms to detect true rain in the same regions as AMSR.

Table 5.3: Comparison of three rain flags: DL SWR rain rate, AMSR SWR rain rate, and the SeaWinds L2B rain impact flag.

Rain Flag	False alarm rate	Missed detection rate
DL SWR	6.82%	41.9%
AMSR SWR	5.7%	42.9%
L2B rain impact flag	0.2%	47%

5.2 Rain Flag Comparison

The SWR algorithms' rain rates can be used to flag wind-only retrievals for rain contamination. This section compares the rain flagging ability of AMSR SWR to the rain impact flag in the SeaWinds L2B file and to the DL SWR rain rates. The two metrics of flagging ability are false alarm rate and missed detection rate. A false alarm occurs when the WVC is flagged for rain but the AMSR rain rate is zero. A missed detection occurs when the WVC is not flagged and AMSR shows a non-zero rain rate. For this comparison rain is detected by a particular algorithm if the rain rate is greater than 0.01 mm/hr.

Table 5.3 contains a summary of the false alarm and missed detection rates for the three rain flags under consideration. The AMSR SWR has a smaller false alarm rate than the DL SWR but has a higher missed detection rate. The difference in both cases is about 1%, indicating that the performance of both algorithms is comparable. The L2B rain impact flag has the lowest false alarm rate and the highest missed detection rate. The L2B flag, which is derived from AMSR data, is asserted when rain has an appreciable impact on the accuracy of wind retrieval. This suggests that the rain rate thresholds of [22] can be updated and calibrated with the L2B rain impact flag to lower the false alarm rate by increasing the missed detection rate (see Section 6.1).

Table 5.4: Comparison of wind retrieval performance of the L2B, DL SWR, and AMSR SWR algorithms against NCEP winds. NCEP wind speeds are multiplied by 0.83.

	Speed (m/s)			Direction (°)		
	Corr. coeff.	Mean diff.	RMS diff.	Corr. coeff.	Mean diff.	RMS diff.
L2B	0.78	-1.29	2.81	0.95	0.98	32
DL SWR	0.85	-0.84	2.21	0.96	0.69	29.1
AMSR SWR	0.83	-0.64	2.26	0.96	1.03	29.4

5.3 Wind Vector Comparison

This section compares the performance of the AMSR SWR wind retrieval to that of the DL SWR using the NCEP winds as a comparison data set. Although NCEP winds have coarse resolution both temporally and spatially, they are not affected by rain. The original SeaWinds wind vectors ("L2B winds") are also included in this analysis to serve as a point of reference. Correlation coefficient, mean difference, and RMS difference of speed and direction with respect to NCEP wind vectors are computed for all three wind vector data sets. To account for the bias between NCEP and SeaWinds wind vectors, NCEP winds are multiplied by 0.83 [3, 7]. Table 5.4 summarizes the comparison. Overall, the performance of both SWR algorithms is comparable. Both SWR algorithms are an improvement over the L2B processing and have comparable performance. The DL SWR performs slightly better than the AMSR SWR in all categories but wind speed bias.

To demonstrate the AMSR SWR's ability to correct rain contamination of wind retrieval, Figure 5.4 shows normalized histograms of the wind speed for AMSR SWR, L2B, and NCEP winds. In regime 0, the three wind data sets have very similar

distributions. In regimes 1 and 2, the AMSR SWR winds are more concentrated around lower wind speeds, indicating that the augmented wind speeds in the L2B winds due to rain contamination are being reduced by the AMSR SWR.

Figure 5.5 shows normalized histograms of the wind direction relative to the satellite track for AMSR SWR, L2B, and NCEP winds. Figure 5.5a represents data in backscatter regime 0 and the distribution of wind speeds is relatively uniform in all directions. Figure 5.5b represents data in regimes 1 and Figure 5.5c represents data in regime 2. There are very large peaks in the L2B histograms at 90° and 270° for regimes 1 and 2, indicating that the retrieved wind has a directional bias in the cross track direction. The NCEP winds also have a directional bias, though not as severe as that of the L2B winds, which is likely due to the fact that NCEP winds are somewhat dependent on L2B winds. The AMSR SWR algorithm corrects this directional bias and reduces it for wind vectors of regimes 1 and 2.

5.4 Qualitative Example: Hurricane Isabel

Hurricane Isabel achieved hurricane status on September 7, 2003 and was a category 5 storm at its strongest intensity. ADEOS II made several passes over the storm before it made landfall on September 18. The intense wind speeds and rain rates present in the storm system allow us to qualitatively assess the performance of the SWR algorithm. Figure 5.6 shows rain rates retrieved by AMSR and AMSR SWR around Isabel on September 16 when it had reduced to a category 3 storm. Although the AMSR SWR measurements are noisy, much of the structure of the rain storm is apparent. The rain bands in the top right corner of the images as well as the area with zero rain rate in the bottom right portion of the storm are captured by the AMSR SWR processing. Certain features are not visible in the AMSR SWR image due to the low resolution and other errors. Though not as accurate as AMSR, the AMSR SWR's rain estimates are useful for observing the structure and extent of rain storms.

Figure 5.7 shows the wind vector fields retrieved by NCEP, AMSR SWR, and L2B processing for the same view of Isabel. Rain contamination is very noticeable

in the L2B wind field (Figure 5.7c), especially above and to the left of the storm center, where many of the wind vectors point across the satellite track. The change in direction of these winds is abrupt at the edges of these rain-contaminated cells. The AMSR SWR winds (Figure 5.7b) have a more continuous, circular flow around the storm center that more closely matches the flow of the NCEP winds (Figure 5.7a). The rain-contaminated cells in the top right corner of the L2B field are also corrected by AMSR SWR processing, resulting in lower wind speeds that are more consistent with the wind speeds of neighboring WVCs and vectors that no longer point across the track.

5.5 Summary

After applying bias correction methods to the AMSR SWR rain model, AMSR SWR rain estimates have a smaller bias than the DL SWR, even though they are less correlated with AMSR rain rates. AMSR SWR rain rates are generally more accurate and precise than those of the DL SWR. The AMSR SWR has a fewer false rain rates than the DL SWR, but it misses more true rain rates. The rain flagging capability of the DL and AMSR SWR algorithms are comparable; however, comparison to the AMSR-derived rain impact flag suggests that the flagging capability can be improved if the SWR rain rate thresholds are properly calibrated. Both SWR algorithms improve the accuracy of wind estimates relative to NCEP winds. DL SWR performs marginally better than the AMSR SWR in all categories except speed bias. The AMSR SWR algorithm corrects the typical effects of rain contamination by lowering artificially high wind speed estimates and by correcting wind vectors that point cross-track due to rain contamination. These corrections were verified by comparing wind speed and direction histograms and were observed qualitatively in the wind fields of Hurricane Isabel.

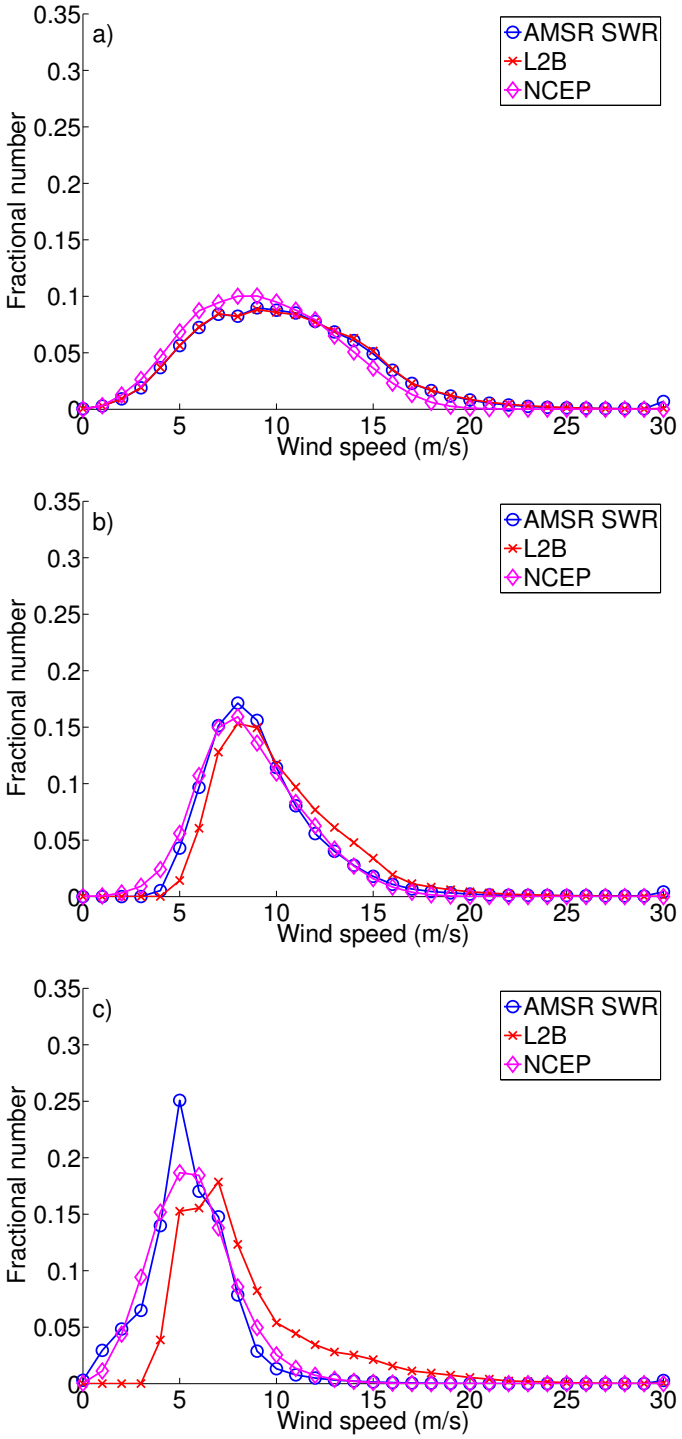

Figure 5.4: Normalized histograms of wind speed of AMSR SWR, L2B, and NCEP winds for a) regime 0, b) regime 1, and c) regime 2. Regime 0 - wind dominates; regime 1 - wind and rain are comparable; regime 2 - rain dominates. Data is from May 2003.

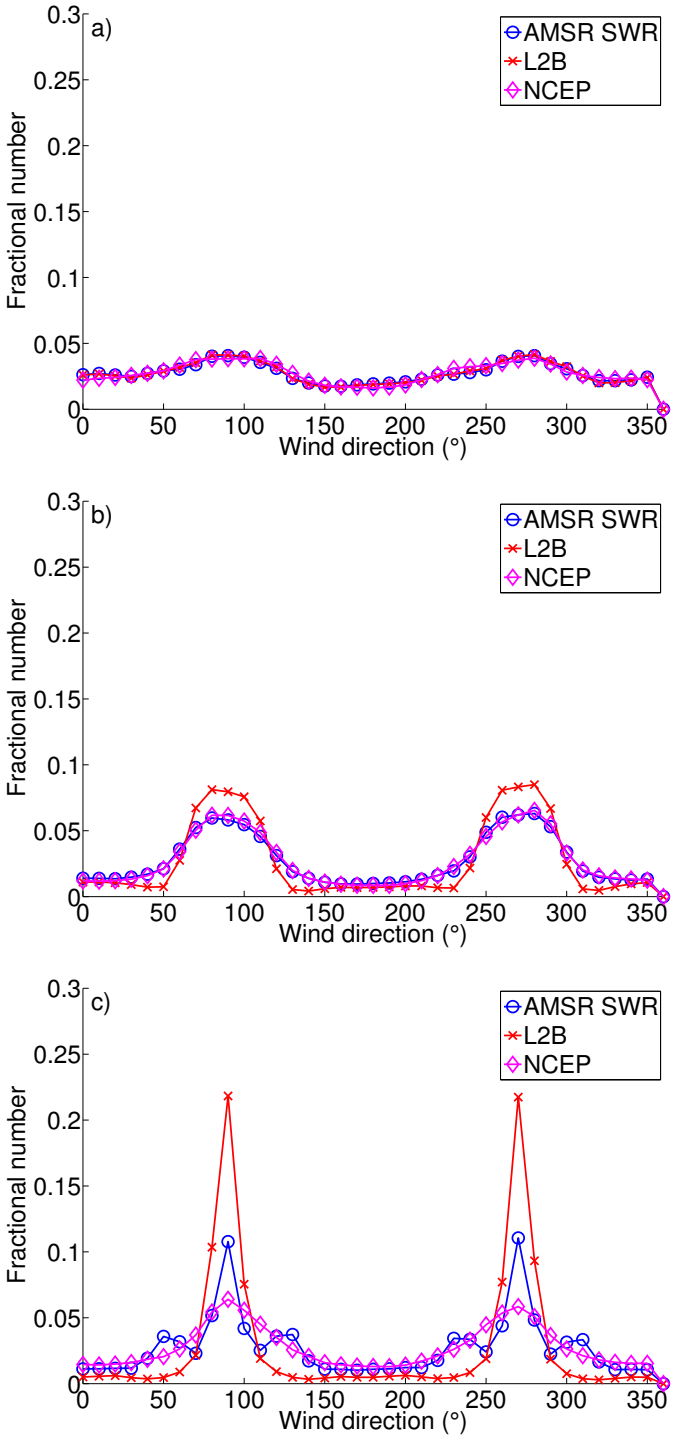

Figure 5.5: Normalized histograms of wind direction of AMSR SWR, L2B, and NCEP winds for a) backscatter regime 0, b) regime 1, and c) regime 2. The direction is relative to the forward satellite track. Regime 0 - wind dominates; regime 1 - wind and rain are comparable; regime 2 - rain dominates. Data is from May 2003.

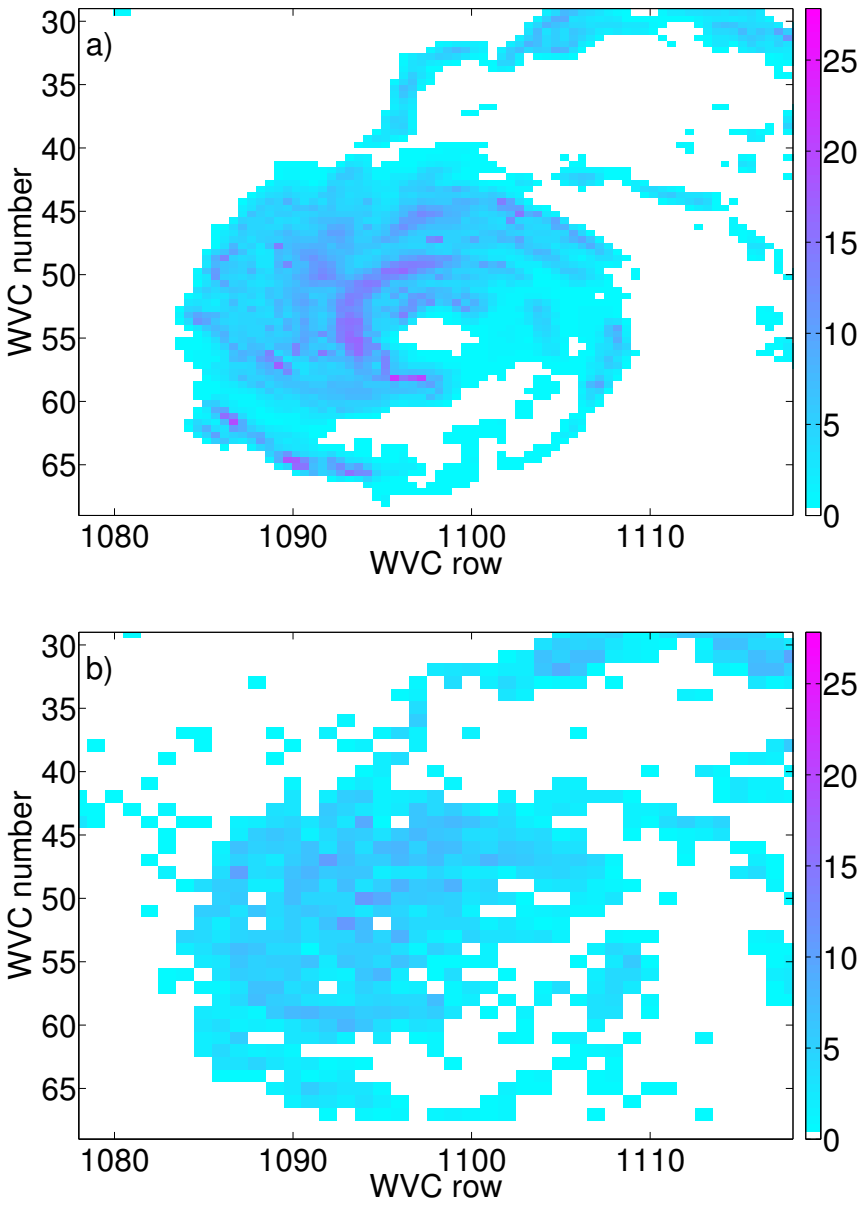

Figure 5.6: Hurricane Isabel rain rates retrieved by a) AMSR and b) AMSR SWR on September 16, 2003 (SeaWinds rev number 3941, JD 259) centered at 27° N latitude and 70° W longitude. Rain rates units are mm/hr.

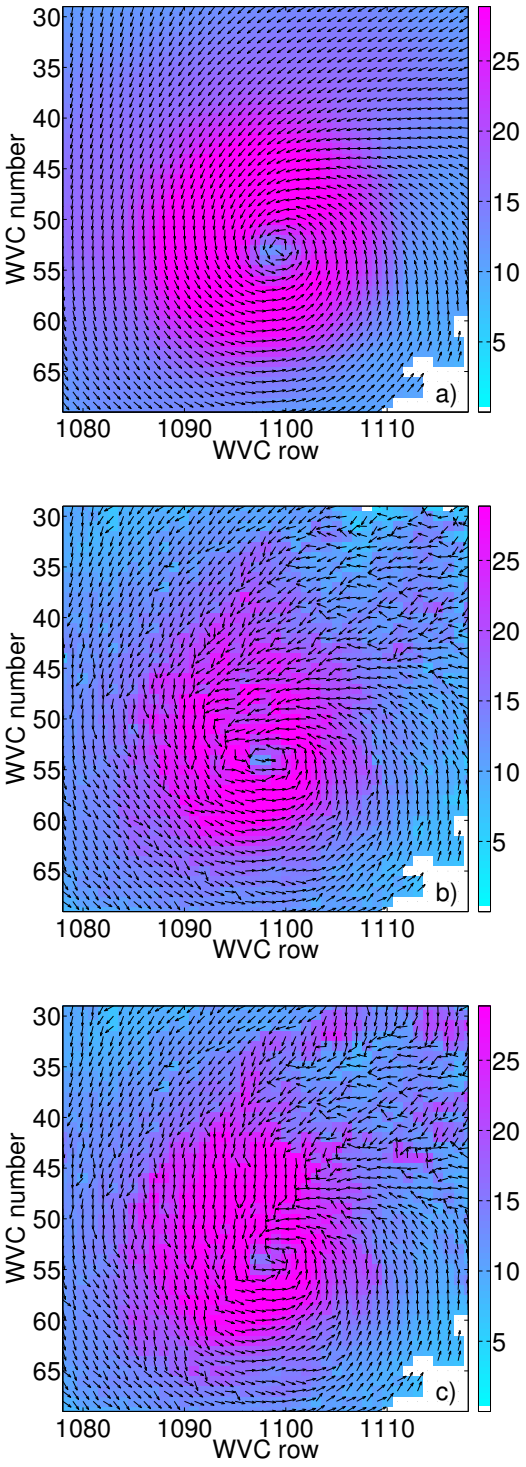

Figure 5.7: Hurricane Isabel wind vectors retrieved by a) NCEP, b) AMSR SWR, and c) SeaWinds L2B processing on September 16, 2003 (SeaWinds rev number 3941, JD 259) centered at 27° N latitude and 70° W longitude. Wind speed units are m/s.

Chapter 6

Conclusion

A wind and rain backscatter model derived from AMSR and SeaWinds on ADEOS II has been implemented in the SWR algorithm. A climatological map of the mean rain height derived from AMSR data is used by the SWR algorithm to produce surface rain rate estimates comparable to those of AMSR. The AMSR SWR rain estimates are an improvement compared to DL SWR rain estimation. They are generally more accurate and precise and have a low false alarm rate. The AMSR SWR also corrects much of the latitude-based errors in rain rate estimates to which the DL SWR was subject. The wind vector correction capability of the algorithm is effective at reducing artificially high wind speeds caused by rain-induced backscatter augmentation. The cross-track wind direction bias caused by rain contamination is significantly reduced and in qualitative comparisons of Hurricane Isabel, the wind field has a more self-consistent flow. Overall, the SWR algorithm is an effective method of improving the accuracy of SeaWinds scatterometer wind retrieval and has the added benefit of retrieving rain rates when radiometer data is not available.

6.1 Recommendations for Future Studies

This thesis represents the first attempt to update the SWR algorithm and calibrate it with AMSR rain data. There are many improvements that can be made to the AMSR SWR algorithm before using it to process SeaWinds on QuikSCAT data. The four parameter MAP estimator presented in Section 4.2.1 was not simulated due to the difficulty of resolving minima in four dimensions and due to the length of time required to compute the objective function. A future study might attempt to simulate

the MAP estimator to compare its performance to the more simplified method chosen for this study. Even though rain height is now accounted for in the rain estimation process, there still appears to be a latitude-based dependence on the AMSR SWR rain rate bias. The model parameter coefficients could be calculated for various latitudes, to make a latitude dependent rain model. The rain height maps developed for this study are limited temporally to only six months worth of data. The AMSR-E, AMSR's successor aboard the NASA Aqua satellite, has been in operation since 2002 and can be used to make more comprehensive climate maps of the rain height. An alternative to this is to create an effective rain height map, where rain heights are determined by the ratio of AMSR SWR integrated rain rate to AMSR surface rain rate. The rain flagging skill of AMSR SWR can be improved by improving the rain rate thresholds and spatial filtering. The rain rate thresholds developed in [22] were based on simulated data. The ADEOS II mission provides a large comparison data set that can be used to develop thresholds based on real scatterometer data.

Bibliography

[1] "A history of scatterometry," http://winds.jpl.nasa.gov/aboutScat/history.cfm, May 2007.

[2] F. J. Wentz and R. W. Spencer, "SSM/I rain retrievals within a unified all-weather ocean algorithm," *Journal of the Atmospheric Sciences*, vol. 55, pp. 1613–1627, May 1998.

[3] D. W. Draper and D. G. Long, "Simultaneous wind and rain retrieval using SeaWinds data," *IEEE Transactions on Geoscience and Remote Sensing*, vol. 42, no. 7, pp. 1411–1423, July 2004.

[4] P. Queffeulou and A. Bentamy, "Comparison between QuikSCAT and altimeter wind speed measurements," in *Proceedings of IEEE International Geoscience and Remote Sensing Symposium*, vol. 1, July 2000, pp. 269–271, 10.1109/IGARSS.2000.860488.

[5] Z. Jelenak, L. N. Connor, and P. S. Chang, "The accuracy of high resolution winds from QuikSCAT," in *Proceedings of IEEE International Geoscience and Remote Sensing Symposium*, 2002, pp. 732–734.

[6] R. N. Hoffman, C. Grassotti, and S. M. Leidner, "SeaWinds validation: Effect of rain as observed by east coast radars," *Journal of Atmospheric and Oceanic Technology*, vol. 21, no. 9, pp. 1364–1377, September 2004.

[7] D. W. Draper and D. G. Long, "Evaluating the effect of rain on seawinds scatterometer measurements," *Journal of Geophysical Research*, vol. 109, 2004.

[8] L. F. Bliven and J. P. Giovanangeli, "Experimental study of microwave scattering from rain- and wind-roughened seas," *International Journal of Remote Sensing*, vol. 14, no. 5, pp. 855–869, 1993.

[9] D. E. Weissman, M. A. Bourassa, and J. Tongue, "Effects of rain rate and wind magnitude on SeaWinds scatterometer wind speed errors," *Journal of Atmospheric and Oceanic Technology*, vol. 19, no. 5, pp. 738–746, May 2002.

[10] R. F. Contreras, W. J. Pland, W. C. Keller, K. Hayes, and J. Nystuen, "Effects of rain on Ku-band backscatter from the ocean," *Journal of Geophysical Research*, vol. 108, no. C5, pp. (34)1–(34)15, 2003.

[11] Z. Yang, S. Tang, , and J. Wu, "An experimental study of rain effects on fine structures of wind waves," *Journal of Physical Oceanography*, vol. 27, no. 3, pp. 419–430, March 1997.

[12] J. N. Huddleston and B. W. Stiles, "A multidimensional histogram rain-flagging technique for SeaWinds on QuikSCAT," in *Proceedings of IEEE International Geoscience and Remote Sensing Symposium*, vol. 3, July 2000, pp. 1232–1234, 10.1109/IGARSS.2000.858077.

[13] C. A. Mears, D. Smith, and F. J. Wentz, "Detecting rain with QuikSCAT," in *Proceedings of IEEE International Geoscience and Remote Sensing Symposium*, vol. 3, July 2000, pp. 1235–1237, doi:10.1109/IGARSS.2000.858078.

[14] M. Portabella and A. Stoffelen, "Rain detection and quality control of seawinds," *Journal of Atmospheric and Oceanic Technology*, vol. 18, no. 7, pp. 1171–1183, July 2001.

[15] B. W. Stiles and S. H. Yueh, "Impact of rain on spaceborne ku-band wind scatterometer data," *IEEE Transactions on Geoscience and Remote Sensing*, vol. 40, no. 9, pp. 1973–1983, September 2002.

[16] K. A. Hilburn, F. J. Wentz, D. K. Smith, and P. D. Ashcroft, "Correcting active scatterometer data for the effects of rain using passive radiometer data," *Journal of Applied Meteorology and Climatology*, vol. 45, pp. 382–398, March 2006.

[17] F. T. Ulaby, R. K. Moore, and A. K. Fung, *Microwave Remote Sensing: Active and Passive*. Artech House, 1981, vol. 1.

[18] F. J. Wentz and D. K. Smith, "A model function for the ocean-normalized radar cross section at 14 GHz derived from NSCAT observations," *Journal of Geophysical Research*, vol. 104, no. C5, pp. 11 499–11 514, May 1999.

[19] *SeaWinds Science Data Product User's Manual, D-21551*, 1st ed., Jet Propulsion Laboratory - California Institute of Technology, July 2002.

[20] B. W. Stiles, B. D. Pollard, and R. S. Dunbar, "Direction interval retireval with thresholded nudging: A method for improving the accuracy of QuikSCAT winds," *IEEE Transactions on Geoscience and Remote Sensing*, vol. 40, no. 1, pp. 79–89, January 2002.

[21] S. J. Shaffer, R. S. Dunbar, S. V. Hsiao, and D. G. Long, "A median-filter-based ambiguity removal algorithm for NSCAT," *IEEE Transactions on Geoscience and Remote Sensing*, vol. 29, no. 1, pp. 167–174, January 1991.

[22] D. W. Draper and D. G. Long, "Assessing the quality of SeaWinds rain measurements," *IEEE Transactions on Geoscience and Remote Sensing*, vol. 42, no. 7, pp. 1424–1432, July 2004.

[23] M. W. Spencer, C. Wu, and D. G. Long, "Tradeoffs in the design of a spaceborne scanning pencil beam scatterometer: Applications to SeaWinds," *IEEE Transactions on Geoscience and Remote Sensing*, vol. 35, no. 1, pp. 115–126, January 1997.

[24] "Data release addendum: Data quality overview," ftp://podaac.jpl.nasa.gov/ocean_wind/quikscat/doc/qs-rlsadd.doc, May 2000, QuikSCAT Project Data Release Notes.

[25] S. Veleva, Personal Communication, October 2006.

[26] ——, Personal Communication, April 2004.

[27] G. Liu and Y. Fu, "The characteristics of tropical precipitation profiles as inferred from satellite radar measurements," *Journal of the Meteorological Society of Japan*, vol. 79, no. 1, pp. 131–143, February 2001.

[28] E. J. Zipser, *Handbook of Weather, Climate, and Water: Dynamics, Climate, Physical Meteorology, Weather Systems, and Measurements.* John Wiley & Sons, Inc., 2003, ch. 30.

[29] M. W. Spencer, C. Wu, and D. G. Long, "Improved resolution backscatter measurements with the SeaWinds pencil-beam scatterometer," *IEEE Transactions on Geoscience and Remote Sensing*, vol. 38, no. 1, pp. 89–104, January 2000.

[30] L. S. Chiu and A. T. C. Chang, "Oceanic rain column height derived from SSM/I," *Journal of Climate*, 2000.

[31] M. Thurai, E. Deguchi, K. Okamoto, and E. Salonen, "Rain height variability in the tropics," *Microwaves, Antennas and Propagation, IEEE Proceedings*, vol. 152, no. 1, pp. 17–23, February 2005.

[32] B. Natarajakumar, "Estimation of rain height from rain rate using regression-based statistical model: Application to SeaWinds on ADEOS-II," Master's thesis, University of Kansas, 2001.

[33] D. Draper, "Wind scatterometry with improved ambiguity selection and rain modeling," Ph.D. dissertation, Brigham Young University, December 2003.

Appendix A

Notes on Rain Model Parameter Calculation

This appendix explains some of the details in calculating the parameters of the rain model discussed in Sections 3.4 and 5.1 of this thesis.

A.1 Adjustment of Atmospheric Rain Attenuation

The empirical attenuation provided in the AMSR L2Ao files includes attenuation due to other atmospheric sources such as water vapor and clouds. Using a simple method, we estimate the attenuation from these other sources and subtract it from the empirical attenuation.

Figure A.1 shows a scatter density plot of the AMSR empirical attenuation versus integrated rain rate (see Figure 3.2) with a 100-point non-parametric fit of the mean attenuation superimposed. The non-rain atmospheric attenuation is estimated to be the value of the attenuation when the integrated rain rate is zero. In order to extrapolate this value, a line is fit to the five points of the non-parametric fit closest to zero rain rate. The constant term of this affine relationship is the average non-rain atmospheric attenuation and is subtracted to obtain the rain-only attenuation. For h-pol the value is 0.29 dB and for v-pol the value is 0.34 dB.

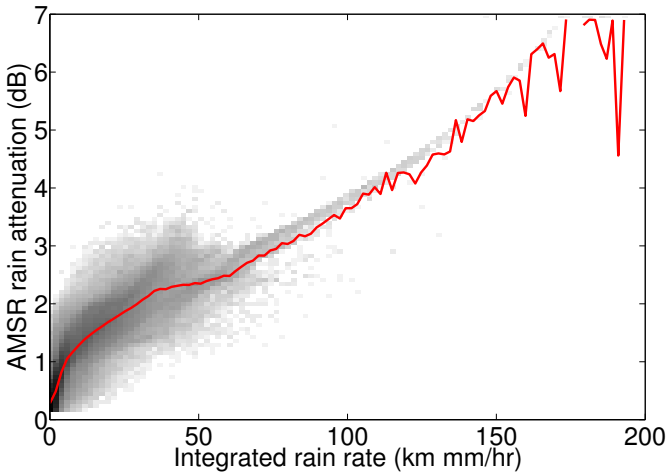

Figure A.1: Scatter density plot of atmospheric rain attenuation (dB) versus integrated rain rate (km mm/hr) for the h-pol beam. The red line represents the mean attenuation for different rain rates.

A.2 Rain Rate Threshold

The AMSR attenuation values are noisy for small integrated rain rates. These data are excluded by means of a rain rate threshold. For this study, the threshold of 1 km mm/hr is used to generate the coefficients of Table 3.1. The coefficients derived from this threshold yield the best rain rate estimates when used in the SWR algorithm compared to other arbitrarily chosen thresholds.

A.3 Bias-corrected Model Coefficients

Section 5.1 indicates that a bias exists in the rain rate estimates when the coefficients of Table 3.1 are used in the SWR algorithm. The bias is corrected using the method discussed in [33] and the bias-corrected coefficients are presented in Table A.1.

Table A.1: Bias-corrected coefficients of the quadratic fits to the parameters α_r and σ_e in Equations (3.15) and (3.16) respectively.

	$c_a(0)$	$c_a(1)$	$c_a(2)$
h-pol	-5.2410	0.4076	0.0167
v-pol	-4.6036	0.4432	0.0171
	$c_e(0)$	$c_e(1)$	$c_e(2)$
h-pol	-24.6335	0.4108	0.0160
v-pol	-24.5579	0.2802	0.0115